

Optimization Hyper-parameter Laws for Large Language Models

Xingyu Xie

XYXIE@NUS.EDU.SG

Department of Mathematics, National University of Singapore, Singapore.

Kuangyu Ding

KUANGYUD@U.NUS.EDU

Department of Mathematics, National University of Singapore, Singapore.

Shuicheng Yan

SHUICHENG.YAN@GMIAL.COM

Skywork AI, Singapore.

Kim-Chuan Toh

MATTOHKC@NUS.EDU.SG

Department of Mathematics and Institute of Operations Research and Analytics, National University of Singapore, Singapore.

Tianwen Wei

WEI.LILLE1@GMAIL.COM

Skywork AI, Beijing.

Abstract

Large Language Models have driven significant AI advancements, yet their training is resource-intensive and highly sensitive to hyper-parameter selection. While scaling laws provide valuable guidance on model size and data requirements, they fall short in choosing dynamic hyper-parameters, such as learning-rate (LR) schedules, that evolve during training. To bridge this gap, we present Optimization Hyper-parameter Laws (Opt-Laws), a framework that effectively captures the relationship between hyper-parameters and training outcomes, enabling the pre-selection of potential optimal schedules. Grounded in stochastic differential equations, Opt-Laws introduce novel mathematical interpretability and offer a robust theoretical foundation for some popular LR schedules. Our extensive validation across diverse model sizes and data scales demonstrates Opt-Laws' ability to accurately predict training loss and identify optimal LR schedule candidates in pre-training, continual training, and fine-tuning scenarios. This approach significantly reduces computational costs while enhancing overall model performance.

Keywords: LLM Efficient Training, Optimization Analysis, Scaling Laws, Convergence Guarantee, Escaping Probability.

1 Introduction

Large Language Models (LLMs) (Achiam et al., 2023; Dubey et al., 2024; DeepSeek-AI et al., 2024) have emerged as a leading paradigm in artificial intelligence, yet their training processes impose significant demands on computational resources and energy. Given the immense scale and associated costs, training these models is typically a one-off endeavor, where crucial hyper-parameters, such as peak learning rate (LR), warmup steps, and LR schedules, must be predetermined and remain fixed throughout the training process. However, determining the optimal values for these hyper-parameters prior to experimentation is often challenging. Inadequate hyper-parameter selection can severely compromise the training process, potentially leading to failure and the consequent waste of computational resources and financial investment.

To address the complexities of hyper-parameter selection in large-scale models, researchers have increasingly relied on **Scaling Laws** (Kaplan et al., 2020; Hoffmann et al., 2022; Achiam et al., 2023). These scaling laws, derived from extensive empirical studies on small-scale models and datasets, provide a practical framework for predicting the relationships between certain hyper-parameters, such as model size and data volume, and training outcomes. By fitting these observed relationships to the power-law formula, scaling laws offer a heuristic approach for extrapolating the expected performance of large-scale models. This enables the selection of model size and data requirements prior to full-scale training, thereby reducing the likelihood of inefficient resource utilization.

While existing research on scaling laws focuses on the relationship between model scale, dataset size and model performance, few studies have explored the scaling law on training hyper-parameters, particularly time-dependent ones like the learning rate schedule. These hyper-parameters, including peak learning rate, are crucial for optimal model performance. Consequently, practitioners often rely on heuristic methods that frequently fall short in addressing the complex challenges of diverse training scenarios.

This challenge extends beyond pre-training. Fine-tuning or continual training of advanced foundation models, such as LLaMA3 (Dubey et al., 2024) or DeepSeek-V2 (DeepSeek-AI et al., 2024), encounters similar difficulties. Although fine-tuning is less computationally expensive than pre-training, the distribution shift between the fine-tuning data and the original training data complicates the selection of optimal hyper-parameters. Furthermore, since the model size is fixed during fine-tuning, scaling laws are not easily applicable. Consequently, the identification of optimal training hyper-parameters, particularly peak LR and warmup steps, typically requires iterative cycles of fine-tuning and evaluation. These hyper-parameters play a crucial role in balancing the retention of the foundation model’s inherent capabilities with its adaptation to new data (Ibrahim et al., 2024).

To address the challenge of hyper-parameter selection in large-scale LLM training, we propose a novel approach termed Optimization Hyper-parameter Laws, **Opt-Laws**. Opt-Laws exploits data gathered from small-scale models and datasets to establish mathematical relationships between training hyper-parameters and final training loss. This enables the pre-selection of suitable hyper-parameter configurations, such as the LR schedule, warmup steps, and peak LR, before commencing large-scale model training or fine-tuning. We first apply stochastic differential equations (SDEs) to model the training dynamics of prevalent first-order optimization algorithms, such as SGD and Adam (Kingma and Ba, 2014), within a continuous-time framework, followed by a detailed analysis of convergence rates and the probability of escaping local minima. This analysis yields a 16-dimensional statistical vector encapsulating key training hyper-parameters, which is subsequently used in a linear regression model to obtain Opt-Laws. *Notably, this work is the first to utilize SDEs in establishing the convergence rate of gradient-based methods for the general non-convex optimization and to apply time-inhomogeneous SDEs for evaluating escape probabilities in non-convex settings.*

Opt-Laws provides mathematical insights into several key phenomena observed in LLM training, such as the greater sensitivity of fine-tuning to warmup steps compared to pre-training, and the trend where larger models necessitate smaller optimal peak LRs. We validate the broad applicability and practical utility of Opt-Laws through extensive numerical experiments conducted on models with over 4 billion (B) parameters and datasets exceeding

450B tokens, encompassing pre-training, continued training, and fine-tuning scenarios. The key contributions are summarized as follows:

- We introduce Opt-Laws, a novel approach that leverages data from small-scale models to effectively capture the relationship between training hyper-parameters and final training loss. By enabling precise predictions of training outcomes for large-scale models, Opt-Laws significantly reduces the computational cost and complexity associated with hyper-parameter tuning.
- By leveraging SDEs, we uncover novel mathematical insights into the model’s convergence dynamics and its capacity to overcome suboptimal local minima, thereby endowing Opt-Laws with a robust and novel theoretical foundation.
- We validate the effectiveness of Opt-Laws through extensive experiments on models with over 4B parameters and datasets exceeding 450B tokens, demonstrating its crucial role in LLM training processes across pre-training, continual training, and fine-tuning.

2 Related Work

2.1 Scaling Laws

The study of scaling laws in LLMs has been essential for understanding how model performance scales with increases in model size, data volume, and computational resources. While early research attempted to model multilayer neural network performance using power laws (Rosenfeld et al., 2020), Kaplan et al. (2020) were the first to apply this approach systematically to LLM training. This foundational work had led to several variations, including the Chinchilla law (Hoffmann et al., 2022; Besiroglu et al., 2024), Mosaic law (Sardana et al., 2024), and models from DeepSeek (Bi et al., 2024) and MiniCPM (Hu et al., 2024), all of which primarily utilize an empirical power law that defines the relationship between training loss, model size N , and data size D in LLMs:

$$\text{Loss} = \underbrace{\frac{A_1}{N^{\kappa_1}}}_{\text{Model-size dependent}} + \underbrace{\frac{A_2}{D^{\kappa_2}}}_{\text{Data-size dependent}} + \underbrace{A_3}_{\text{Irreducible}},$$

where $\kappa_1, \kappa_2 > 0$ represent the scaling exponents, $A_1, A_2 > 0$ are coefficients, and $A_3 \in \mathbb{R}$ denotes the irreducible loss component. Recent studies (Muennighoff et al., 2024; Goyal et al., 2024) have highlighted the impact of data repetition and quality on scaling behavior, suggesting the need for more frequent updates to existing scaling laws. Some researchers have also questioned the sufficiency of power law models, advocating for more complex parameterizations to better capture the relationship between model size and data volume (Hernandez et al., 2021; Caballero et al., 2023). Other studies have extended power laws to model the relationship between training loss and individual hyper-parameters, such as batch size (DeepSeek-AI et al., 2024). Additionally, scaling laws have been applied in downstream task losses (Dubey et al., 2024) or later stages of model alignment, such as fine-tuning (Isik et al., 2024) and RLHF (Gao et al., 2023). A key limitation of these scaling laws is that, while they offer insights into optimal model and data sizes, they lack practical guidance on selecting training hyper-parameters to achieve optimal performance in specific

configurations. Opt-Laws addresses this gap by linking training loss to hyper-parameters, thus enabling the simultaneous selection of model size, data volume, and LLM training hyper-parameters.

2.2 Convergence Analysis via Dynamical Systems

Dynamical systems are powerful tools in the convergence analysis of optimization algorithms. Over the past decade, numerous studies such as [Su et al. \(2014\)](#); [May \(2017\)](#); [Attouch et al. \(2018\)](#); [Muehlebach and Jordan \(2019\)](#); [Attouch et al. \(2024\)](#) have utilized ordinary differential equations (ODEs) to analyze algorithmic convergence properties, particularly employing high-order (with order ≥ 2) ODEs to intuitively interpret the mystery behind momentum acceleration, such as Polyak’s heavy ball method ([Polyak, 1987](#)) and Nesterov’s acceleration ([Nesterov, 1983](#)) in smooth convex optimization problems. In the realm of non-smooth non-convex optimization, differential inclusions, which are more general than ODEs, have recently been applied to establish the convergence of subgradient methods ([Duchi and Ruan, 2018](#); [Davis et al., 2020](#); [Xiao et al., 2024](#); [Ding and Toh, 2024](#)). In addition to ODE-based methods, recent studies ([Gess and Kassing, 2023](#); [Maulen-Soto et al., 2022, 2024](#)) have started using SDEs to derive convergence rates for stochastic gradient methods in convex optimization problems or non-convex optimization problem under Polyak-Łojasiewicz (PL) condition. However, to the best of our knowledge, no SDE-based approach has been established for determining convergence rates in the general non-convex settings. *Our work is the first to apply SDEs in establishing convergence rates for the general non-convex problems, with our derived bounds applicable to any general learning rate policy, without relying on specific patterns, such as constant, sublinearly decaying, or linearly decaying learning rates.*

2.3 Escaping analysis via SDEs

A closely related research area involves analyzing SGD’s escape dynamics using SDEs ([Nguyen et al., 2019](#); [Xie et al., 2020](#); [Mori et al., 2022](#); [Ibayashi and Imaizumi, 2023](#); [Battash et al., 2024](#)). These work focus on estimating the exit time, which measures how quickly an SGD sequence can move from a sharp local minimum to a flatter region, potentially improving generalization performance ([Keskar et al., 2016](#); [Foret et al., 2020](#)). The classic Eyring-Kramers law ([Kramers, 1940](#); [Berglund, 2013](#)), based on large deviation theory, is typically used for such exit time estimations. However, this approach is not directly applicable in our case due to the time-inhomogeneity of the SDEs, which arises from the time-dependent learning rate schedule. To address this challenge, we employ a Gaussian approximation to make the escape analysis more tractable under mild conditions.

3 Optimization Hyper-parameter Laws

To facilitate the understanding of Opt-Laws, we begin this section by presenting a special case where the model size is fixed. Following this, we explore the utilization of Opt-Laws and use it to explain some intriguing phenomena observed in LLM training. In the subsequent [Sec. 4](#), we will extend Opt-Laws to its more general form.

3.1 Opt-Laws with Fixed Model Size

We proposed the Opt-Laws in Eqn. (1) to predict the training loss for LLMs. It is important to note that, in most instances, the training loss of LLMs closely approximates the validation loss. This is because the training epoch for both pre-training and continual training is typically set to one. In this section, we fix the model size and consider the LR schedule $\eta(t) \geq 0$ for all $t \in [0, S]$, where η_{\max} denotes the peak LR, and S represents the total training steps (proportional to data size D such that $D = S \times \text{Batch size} \times \text{Token length}$). The function $\eta(t)$ is defined as $\eta(\Delta_t k) = \eta_k$, where η_k is the LR used at the k -th training step, and Δ_t is a sufficiently small time step. This mapping effectively links each step-index to its corresponding LR.

For simplicity, we set the initial and final values of η_t to zero, i.e., $\eta(0) = \eta(S) = 0$, though these values can be adjusted based on practical requirements. Under these conditions, the training loss and training hyper-parameters adhere closely to the following relationship:

$$\log(\text{Loss}) = \underbrace{c_1 \left(\int_0^a \eta(s) ds \right)^{-\alpha_1} + c_2 \left(\int_a^S \eta(s) ds \right)^{-\alpha_2}}_{\text{convergence speed}} + \underbrace{\frac{c_3}{S} + b}_{\text{bias}} + \underbrace{c_4 \left(\int_0^a (\eta'(s))^2 ds \right)^{\alpha_3} + c_5 \left(\int_a^S (\eta'(s))^2 ds \right)^{\alpha_4}}_{\text{ease of escaping local region}} \quad (1)$$

where a denotes the warmup duration, $\eta'(s)$ is the time derivative of $\eta(s)$, the constants $c_1, c_2, c_3, c_4, c_5, \alpha_1, \alpha_2, \alpha_3, \alpha_4 > 0$, and $b \in \mathbb{R}$ are all dependents on the model and training data. Analogous to scaling laws, Opt-Laws is first parameterized by fitting its constants and power terms on a small-scale model with a similar network architecture and a small subset of the dataset. The parameterized Opt-Laws can then be applied to choosing hyper-parameters in large-scale training. The details on the parameters fitting are clarified in Secs. 3.2 and 4.3.

The first component in Eqn. (1) addresses the convergence speed, elucidating the impact of the LR schedule $\eta(t)$ on optimization convergence. Given the same computational budget, training dynamics with faster convergence tend to achieve lower training loss, thereby enhancing overall efficiency. Notably, the loss is inversely proportional to $\int_a^S \eta_t$, suggesting that, within certain bounds, a higher peak LR can be beneficial (Xie et al., 2024b). However, an excessively high peak LR can also increase the integral $\int_a^S \eta_t'^2$, indicating the need to carefully balance the benefits of a high peak LR against the potential drawbacks. Note that for convenience, we use notation such as $\int_a^S \eta_t'^2$ to denote $\int_a^S (\eta'(t))^2 dt$ in the previous sentence and other parts of this paper.

The third component Eqn. (1) pertains to the negative likelihood of the training trajectory escaping a local region containing at least one local minimum. A well-calibrated $\eta(t)$ is essential for enabling the training dynamics to overcome suboptimal local minima and guide the model toward a more favorable solution landscape. Furthermore, the loss is proportional to $\int_0^a \eta_t'^2$ and $\int_a^S \eta_t'^2$, meaning that overly rapid warmup or cooldown phases can lead to poorer loss outcomes. This observation aligns with the empirical findings in LLM training (Hu et al., 2024). The proposed Opt-Laws quantifies the impact of hyper-parameters, particularly the LR schedule $\eta(t)$ on the loss function. It offers a clear metric to evaluate the

effectiveness of different hyper-parameter combinations. After determining the parameters of Opt-Laws, the following applications are possible:

(1) **Pre-training:** Opt-Laws enable precise selection of training parameters such as LR schedules, peak LR, and cooldown duration. Given the high computational costs of large-scale pre-training, Opt-Laws help avoid costly trial-and-error by providing data-driven guidance, ensuring that the model is trained efficiently from the outset.

(2) **Fine-Tuning:** During fine-tuning, especially on small datasets, Opt-Laws assist in selecting optimal warmup steps and LRs. This reduces the risk of overfitting or underfitting, which is critical when adjusting the model to new, limited data without compromising its generalization capabilities.

(3) **Continual Training:** In continual training, where models are continuously updated with new data, Opt-Laws provide a framework for adjusting key hyper-parameters. By leveraging insights from pre-training, Opt-Laws ensure smooth adaptation to new data, maintaining model performance and stability over time.

3.2 Opt-Laws Parameters Fitting

In Sec. 6, we **validate** the effectiveness of Opt-Laws using numerical formulas on large-scale models and datasets in the *hold-out and out-of-distribution experiment settings*, specifically on unseen large-scale test cases. The fitted coefficients and power terms used in Opt-Laws for these settings are detailed in Appendix Sec. A. Here, we present a small-scale experiment for qualitative discussion, illustrating the potential of Opt-Laws in understanding intriguing phenomena observed during LLM training.

We apply Opt-Laws in Eqn. (1) to fit the training loss of an $8 \times 0.1\text{B}$ MoE model (Zhao et al., 2024; Wei et al., 2024). The decision to use an MoE model over a dense model is based on two key factors: (1) many state-of-the-art LLMs (Achiam et al., 2023; DeepSeek-AI et al., 2024; Reid et al., 2024; Yang et al., 2024; Bai et al., 2023) employ MoE architectures, reflecting current trends, and (2) MoE models are computationally more efficient, allowing faster experimentation within our computational constraints. In this experiment, we fix the model and batch sizes (both with a token length and batch size of 1024) while varying the token quantities from the RedPajama-v2 dataset (Computer, 2023): 3B, 6B, 10B, and 30B tokens. We adjust the warmup steps and peak LRs to analyze their impact on final loss. The LR schedule $\eta(t)$ linearly increases to a peak LR η_{\max} during warmup, followed by a linear decay to zero in the cooldown phase. The warmup steps are denoted by a .

The fitting error of Opt-Laws was kept below 0.5%, making the predicted loss nearly identical to the actual loss. The results are illustrated in the contour plot in Fig. 1, which demonstrates that as the training data size increases, the optimal hyper-parameter range expands. This implies that with sufficient data, model training becomes more robust to hyper-parameter variations. Additionally, the impact of warmup steps on the final results decreases as the data size increases, corroborating the numerical observations from Gupta et al. (2023); Ibrahim et al. (2024). However, it is critical to ensure that the warmup steps are not too small, as this can cause a sharp increase in training loss, evident on the left side of the plots in Fig. 1.

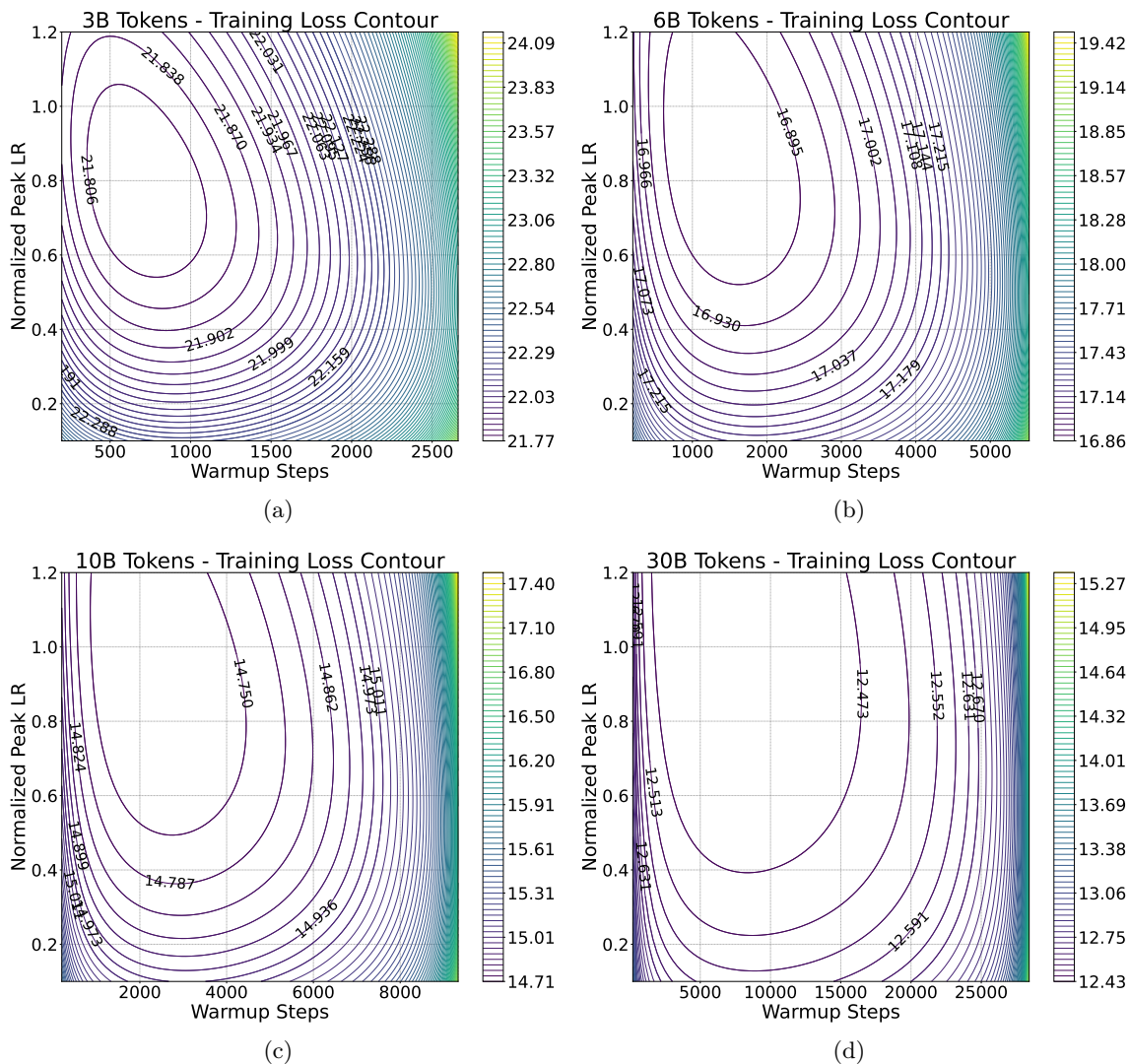


Figure 1: Contour plots of predicted perplexity, which is the exponential of the predicted training loss, versus warmup steps and peak LR for different token quantities (3B, 6B, 10B, 30B) from the RedPajama-v2 dataset.

3.3 Understanding Training Phenomena through Opt-Laws

With the proposed Opt-Laws, many previously interesting observations in practical LLM training become comprehensible.

3.3.1 INFLUENCE OF WARMUP STEPS ON TRAINING LOSS

Recent research has demonstrated that the number of warmup steps exerts a negligible effect on the final training loss, particularly in the context of continual training. For example, studies (Ibrahim et al., 2024; Gupta et al., 2023) on dense models with around 0.5B parameters, trained on over 100B tokens, have observed that variations in linear warmup steps result in only marginal differences in the final loss. This finding is consistent with our

results in Fig. 1 (d). When the token count is sufficiently large and surpasses the Chinchilla Scaling Law (25.6 tokens per parameter) (Hoffmann et al., 2022; Besiroglu et al., 2024), the range of effective warmup steps broadens significantly, rendering the final loss relatively insensitive to changes in warmup duration.

This observation does not contradict other studies (Lv et al., 2023; Jin et al., 2023) that emphasize the need for careful tuning of warmup steps. Such sensitivity is primarily seen during fine-tuning, where the token-to-parameter ratio is much lower than the value suggested by the Chinchilla Scaling Law. This aligns with our findings in Fig. 1 (a) and Fig. 1 (b), which show a narrower optimal range for warmup steps. Consequently, fluctuations in loss due to variations in the warmup steps are more likely to occur during fine-tuning.

3.3.2 INSIGHTS INTO LR SCHEDULE EFFECTS THROUGH OPT-LAWS

OpenAI researchers previously observed that the LR schedule $\eta(t)$ has a negligible impact on the final training loss (Kaplan et al., 2020). However, recent studies on pre-training and continual training of LLMs have discovered new LR schedules that achieve lower training losses compared to the widely-used cosine decay schedule (Ibrahim et al., 2024; Hägele et al., 2024). These seemingly contradictory findings can be reconciled through our Opt-Laws.

Opt-Laws reveal that the model loss has an asymptotic lower bound related to the model capability. When the dataset is sufficiently large, the training loss approaches this asymptotic bound, rendering it independent of the LR schedule. However, the rate at which the loss approaches this bound is influenced by the LR schedule $\eta(t)$. This explains why, during fine-tuning or continual training, it is possible to find some LR schedules that outperform cosine decay: these newly discovered schedules enable the model to reach its performance limits more rapidly. Yet, as the dataset size increases, the differences introduced by varying LR schedules diminish.

To further elucidate this asymptotic behavior, we will now consider two specific scenarios to derive the precise expressions of the Opt-Laws. The first is the classical linear warmup followed by cosine decay. In this schedule, the LR is linearly increased to η_{\max} over a steps, and then decays to zero in a cosine fashion.

$$\eta_{\cos}(t) = \begin{cases} \eta_{\max} \cdot \frac{t}{a} & t \in [0, a] & \text{(warmup)}, \\ \frac{\eta_{\max}}{2} \cdot \left(\cos\left(\pi \cdot \frac{t-a}{S-a}\right) + 1 \right) & t \in [a, S] & \text{(cooldown)}, \end{cases} \quad (2)$$

where a is the linear warmup steps, and S represents the total training steps. The second schedule has gained popularity in the recent continual training of LLMs, as evidenced in the work (Hu et al., 2024; Hägele et al., 2024). In this strategy, the LR is linearly increased to η_{\max} , held constant for a period, and then rapidly decayed to the minimum value. For simplicity, we model the decay as a linear decrease to zero.

$$\eta_{\text{const}}(t) = \begin{cases} \eta_{\max} \cdot \frac{t}{a} & t \in [0, a] & \text{(warmup)}, \\ \eta_{\max} & t \in [a, a_c] & \text{(constant)}, \\ \eta_{\max} \cdot \left(1 - \frac{t-a_c}{S-a_c} \right) & t \in [a_c, S] & \text{(cooldown)} \end{cases} . \quad (3)$$

Here, $a_c - a$ represents the duration of the constant LR phase, and $S - a_c$ is the period over which the LR linearly decays to zero. In Opt-Laws Eqn. (1), we incorporate the constant

LR phase into the cooldown phase for simplification. For more complex LR schedules, the distinction between the warmup phase and other phases is elaborated in Sec 4.3. We can derive the following proposition, which demonstrates that as the data size increases, the difference between η_{cos} and η_{const} diminishes under Opt-Laws($\eta(\cdot)$), which we define as $\log(\text{Loss})$ in Eqn. (1).

Proposition 1 *Let $a = r_a S$ and $a_c = r_{a_c} S$. For any $r_a > 0$ and $r_{a_c} > 0$ such that $0 < r_a \leq r_{a_c} < 1$, it holds that*

$$\lim_{S \rightarrow \infty} |\text{Opt-Laws}(\eta_{\text{cos}}(\cdot)) - \text{Opt-Laws}(\eta_{\text{const}}(\cdot))| = 0.$$

If we set $a = 0.01S$ and $a_c = 0.85S$ (as recommended by Hu et al. (2024)), we observe that when S is relatively small, $\eta_{\text{const}}(\cdot)$ yields a lower Opt-Laws value because the integral $\int_a^S \eta_{\text{const}}(s) ds$ is larger. This results in a lower loss for the same amount of data compared to $\eta_{\text{cos}}(t)$, consistent with findings in Hu et al. (2024) and Hägele et al. (2024). However, in the special case where $a = a_c$, meaning there is no constant phase for $\eta_{\text{const}}(t)$, the results reverse, with $\text{Opt-Laws}(\eta_{\text{cos}}) > \text{Opt-Laws}(\eta_{\text{const}})$, aligning with our experimental outcomes (see Sec. 6 for more details).

However, as S becomes sufficiently large, the Opt-Laws for both LR schedules asymptotically converge to a fixed value. This value depends solely on the model capacity and data property, and is independent of the specific LR schedule. This explains why some studies claim that the choice of LR schedule is mostly irrelevant to the final performance. The study Kaplan et al. (2020) validated the impact of LR schedules on loss using small models (with only 3M learnable parameters) and large datasets. In such scenarios, the model loss is already very close to its asymptotic limit, making it difficult to observe the effect of optimization hyper-parameters.

To further validate the insights provided by Opt-Laws regarding the impact of LR schedules on training loss, we conducted practical experiments comparing three different LR schedules under both low and high data volume settings. Detailed experimental results and methodologies are presented in Sec. 6.1. The empirical results align with the predictions of Opt-Laws. When the data volume is small (i.e., S is small), the final loss decreases with longer durations of high learning rates, indicating that such LR schedules are more effective in low-data regimes. However, as S increases, the differences in final loss between different LR schedules become negligible. This confirms Opt-Laws’s conclusion that while LR schedules have a significant impact when data is limited, their influence fades as the dataset size grows and the model loss approaches its asymptotic limit.

4 Extension to the General Cases

This section aims to extend the Opt-Laws to more general scenarios by explicitly incorporating model size into its formulation. To this end, we conducted a series of controlled experiments to evaluate the effects of various training parameters on the final training loss.

We standardize the optimizer and LR schedule (linear warmup followed by linear cooldown). Subsequently, we performed grid experiments across a range of model sizes, LRs, warmup steps, and data sizes. Specific details on the MoE configurations, like layers number, hidden size, training settings, etc., are provided in Sec. A. The results of these experiments

are summarized in Fig. 2, where each grid point represents the smoothed final training loss for the corresponding setting. In cases where training diverged, the loss was consistently set to 7, reflecting the typical plateau observed in practice. The experimental results show significant variability in the training loss across different hyper-parameter configurations, even with fixed model and data sizes, variability that existing scaling laws fail to capture. Unlike the Opt-Laws in Eqn. (1), this generalized scenario includes cases of training divergence and reveals that the loss is not continuous across different hyper-parameter combinations, underscoring the complexity of generalizing Opt-Laws.

To address these challenges, we first propose a computational framework that predicts training divergence based on peak LR, warmup steps, model size, and data size. Then for non-divergent configurations, we extend Opt-Laws to incorporate model size, enabling precise estimation of final training loss before training begins.

4.1 Predicting Training Divergence

We first discuss the selection of hyper-parameters to prevent training divergence. Fig. 2 provides two key insights: (1) Excessively high peak LRs can cause divergence, but increasing the warmup duration can prevent this, to make training stable. (2) The hyper-parameter combinations that lead to divergence vary, depending on the model and data size.

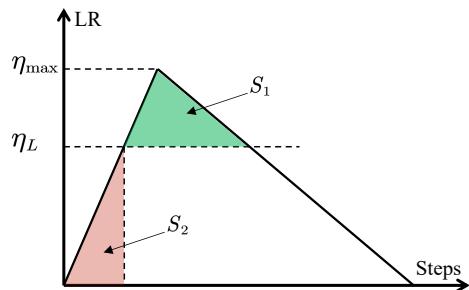


Figure 3: Illustration of the criterion for predicting training divergence using a linear warmup and cooldown schedule. The areas S_1 (where the learning rate is below the threshold η_L) and S_2 (where it exceeds η_L) are compared. A ratio $S_1/S_2 > 1$ suggests stable training, while a ratio < 1 indicates likely divergence.

For general non-convex optimization problems $\min_{\mathbf{x}} f(\mathbf{x})$, optimization theory typically dictates that the peak LR η_{\max} should not exceed $2/L$, where L is the Lipschitz constant of the function gradient $\nabla f(\cdot)$, regardless of the LR schedule (Arjevani et al., 2022; Xie et al., 2024b; Rotaru et al., 2024). However, estimating the Lipschitz constant for neural networks remains an open challenge (Kim et al., 2021; Khromov and Singh, 2024). Moreover, recent studies indicate that surpassing certain theoretical thresholds for peak LRs does not necessarily lead to divergence; rather, when appropriately managed, peak LRs above $2/L$ can even enhance convergence (Grimmer et al., 2024).

From these observations, we hypothesize that training divergence is not merely a consequence of an excessively large η_{\max} . Instead, it is influenced by the duration that the LR remains above a critical threshold η_L and the length of the warmup phase. Ideally, η_L would correspond to $2/L$, where L is the Lipschitz constant of the function gradient. For neural networks, L tends to increase with model size (Khromov and Singh, 2024), suggesting that η_L should decrease as the model size grows. However, with larger datasets, η_L can actually increase because the greater data volume allows the training dynamics more time to correct the negative effects of an excessively high peak LR, as illustrated in Fig. 2. Based on this intuition, we let $\eta_L = \mathcal{O}(S^{\hat{\alpha}_1}/N^{\hat{\alpha}_2})$, where $\hat{\alpha}_1, \hat{\alpha}_2 > 0$ are data-driven

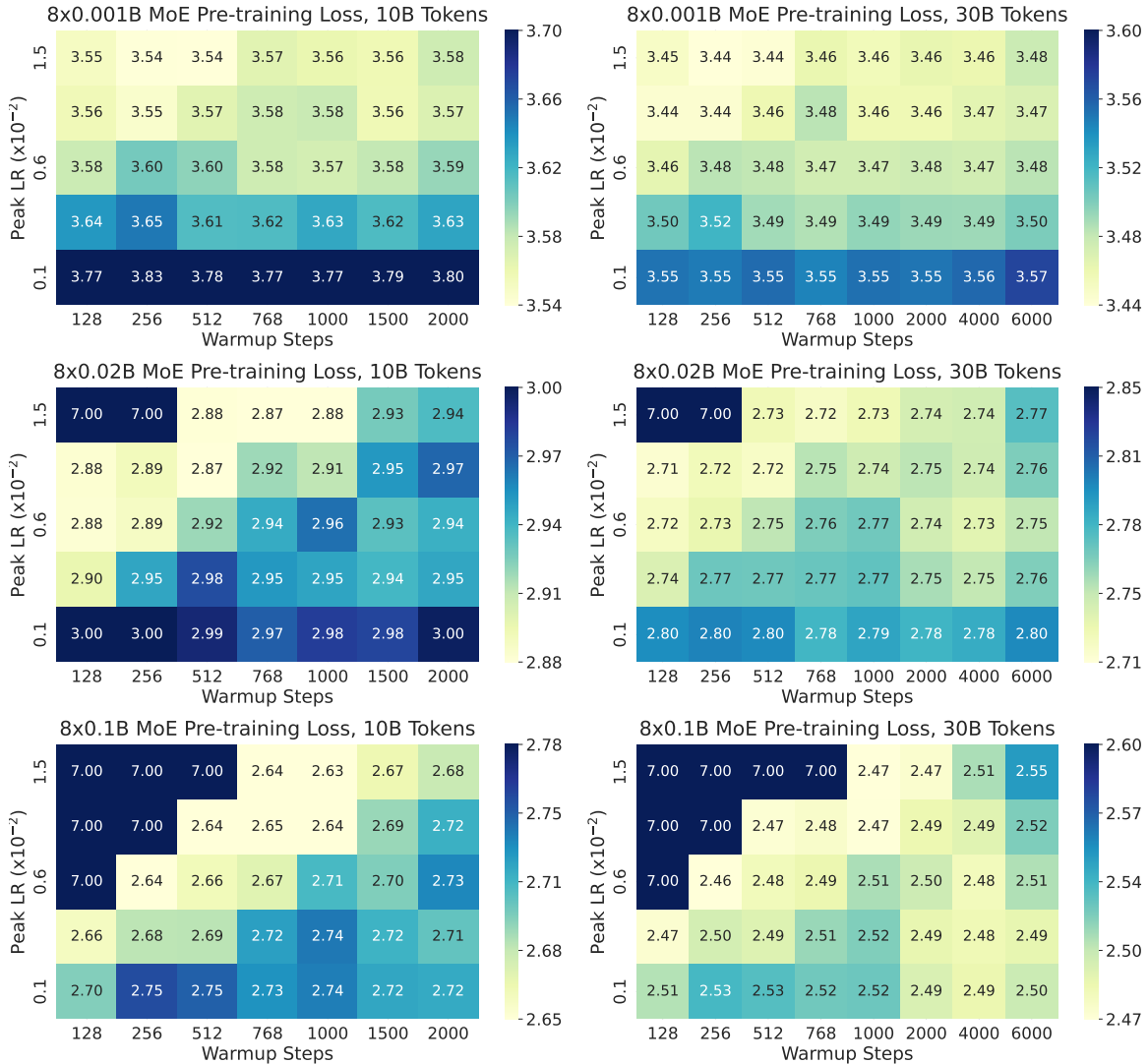


Figure 2: Smoothed final training loss across various combinations of training parameters, including model sizes from $8 \times 0.001\text{B}$ to $8 \times 0.3\text{B}$ MoEs, peak LRs from $1\text{e-}3$ to $1.5\text{e-}2$, warmup steps from 128 to 6000, and data sizes of 10B and 30B tokens. Each grid point represents the loss for a specific parameter set. Divergent training runs were assigned a loss of 7, reflecting the typical plateau observed in practice.

constants, S is the number of iterations (proportional to data size), and N is the model size (i.e., the number of learnable parameters).

It is important to note that whether training diverges is not solely determined by η_L ; the duration of the warmup phase also plays a significant role. Building on these insights, we propose evaluating the ratio of the integral during the effective warmup phase (where LR is below η_L) to the integral during the phase where LR exceeds η_L . This ratio serves as a criterion for predicting whether a given combination of hyper-parameters will lead to training divergence. For instance, in a linear warmup and cooldown schedule (as shown in Fig. 3), we check whether the area ratio S_1/S_2 exceeds 1 to predict training success.

Specifically, we define:

$$R(\eta_{\max}, a_1, N, S) := \frac{S(\eta_{\max} - \eta_L)^2}{\hat{c}_3 a_1 \eta_L^2}, \quad \eta_L := \min(\eta_{\max}, \frac{\hat{c}_1 S^{\hat{\alpha}_1}}{\hat{c}_2 N^{\hat{\alpha}_2}}), \quad (4)$$

where S is the iteration number, N is the model size, a_1 is the number of warmup steps, and $\hat{c}_1 > 0$, $\hat{c}_2 > 0$, $\hat{c}_3 > 0$, $\hat{\alpha}_1 > 0$, and $\hat{\alpha}_2 > 0$ are data-driven parameters. Similar to the Opt-Laws approach, these parameters are estimated by fitting the real data presented in Fig. 2, with the fitted values provided in Appendix Sec. A. We find that if $R(\eta_{\max}, a_1, N, S) > 1$, indicating that the time spent above η_L is too long relative to the effective warmup duration, training is likely to fail. Conversely, if $R(\eta_{\max}, a_1, N, S) < 1$, the chosen hyper-parameters are unlikely to cause divergence. In Eqn. (4), η_L is inversely related to model size and directly proportional to data size, implying that larger models require lower peak LR, while larger datasets may permit a higher peak LR. This observation aligns with established practices in training modern LLMs, such as LLaMAs (Dubey et al., 2024).

As shown in Fig. 5, the $R(\eta_{\max}, a_1, N, S)$ metric effectively predicts training outcomes across various data sizes, model sizes, and hyper-parameter combinations. In the figure, we do not directly report the R values; instead, for scenarios where $R > 1$, which indicates a high likelihood of training divergence, we assign a fixed value of 7. This assignment clearly marks cases expected to fail, facilitating a clear distinction between successful and divergent training outcomes. The 100% prediction accuracy observed in Fig. 5 is not a result of overfitting, as only two-thirds of the grid data points were used for parameter fitting, with the remaining one-third reserved for validation. Notably, the metric R consistently predicts training divergence regardless of whether the data was used for fitting or validation.

4.2 Generalized Opt-Laws

In this section, we extend the Opt-Laws from Eqn.(1) by incorporating model size into the formulation. As shown in Fig. 2, the final training loss exhibits non-smooth variations across different hyper-parameter combinations. For example, in the "8x0.1B MoE with 10B Tokens" setting, both warmup = 256, $\eta_{\max} = 6 \times 10^{-3}$ and warmup = 512, $\eta_{\max} = 9 \times 10^{-3}$ achieve a low final loss of 2.64. However, slight perturbations, such as warmup = 512, $\eta_{\max} = 6 \times 10^{-3}$, result in a suboptimal loss of 2.66. Additionally, some combinations, like warmup = 256, $\eta_{\max} = 9 \times 10^{-3}$, can even cause training divergence. Unlike the Opt-Laws in Eqn. (1), the loss here cannot be captured by a simple linear combination of smooth, monotonic basis functions, as the loss landscape is multi-modal with respect to hyper-parameters.

To enhance the flexibility and expressiveness of the Opt-Laws, we consider combining basis functions through multiplication to create new functions that more accurately describe the training dynamics. The basis functions are related to the convergence rate of optimization algorithms and their ability to escape local minima during training. Given a LR schedule $\eta(t)$, the convergence rate of typical first-order stochastic optimization algorithms (e.g., SGD, Adam) is influenced by (see Sec. 5 Theorems 1 and 2)

$$\text{Convergence Bound} \propto \left[\frac{N}{\int_0^{a_{c_1}} \eta(t) dt}, \frac{N}{\int_{a_{c_2}}^S \eta(t) dt} \right], \quad (5)$$

where the convergence bound represents the average gradient norm, usually serving as an indicator of how near the current loss is to a local minimum in continuous optimization, S

represents the number of iterations, N is the model size, and $a_{c_1} \leq a_{c_2}$ are specific points within the interval $[0, S]$ that define the divisions in the LR schedule. The “proportional to” \propto indicates that the convergence bound is influenced by these basis functions in Eqn. (5). Specifically, when the values of these functions are smaller for a given $\eta(t)$, the optimization algorithm tends to converge more quickly to a stationary point.

Typically, a_{c_1} marks the end of the warmup phase, and a_{c_2} indicates the start of the cooldown phase. We segment the LR schedule into multiple phases because some intermediate phases have a negligible effect on the final training loss and are therefore excluded from loss fitting. This aligns with findings by Ibrahim et al. (2024), who observed that as long as the warmup and cooldown are properly configured, LR schedules with periodic cycles, where the rate repeatedly rises and falls, result in final losses similar to those with a linear warmup followed by inv-sqrt cooldown. This suggests that LR variations during certain intermediate phases do not significantly affect the final loss.

In addition to convergence complexity, the probability of remaining trapped in a local region for stochastic optimization algorithms is also related to the following quantities (see Sec. 5 Theorems 3 and 4):

$$\text{Trapping Probability} \propto \left[\frac{1}{SN}, \int_0^{a_{e_1}} \eta'(t)^2 dt, \int_{a_{e_2}}^S \eta'(t)^2 dt \right], \quad (6)$$

where N is the model size, and $a_{e_1} \leq a_{e_2}$ are values between 0 and S . Similar to the previous Eqn. (5), smaller values of these basis functions in Eqn. (6) indicate a higher probability of escaping a local region under the chosen $\eta(t)$.

To extend the Opt-Laws, we consider pairwise combinations of the basis functions from Eqn. (5) and Eqn. (6). We introduce three sets of terms: the convergence term $C(\eta_t, \mathbf{a}_c, S, N, \boldsymbol{\alpha})$:

$$C(\eta_t, \mathbf{a}_c, S, N, \boldsymbol{\alpha}) := \left[\frac{1}{\int_0^{a_{c_1}} \eta_t}, \frac{1}{\int_{a_{c_2}}^S \eta_t}, \left(\frac{N}{\int_{a_{c_2}}^S \eta_t} \right)^{\alpha_1}, \left(\frac{1}{\int_0^{a_{c_1}} \eta_t \int_{a_{c_2}}^S \eta_t} \right)^{\alpha_2} \right],$$

where $\boldsymbol{\alpha}$ is a predefined vector representing the powers of certain basis functions; the escaping local region term $E(\eta_t, a_e, S, N, \boldsymbol{\alpha})$:

$$E(\eta_t, a_e, S, N, \boldsymbol{\alpha}) := \left[\int_{a_{e_2}}^S \eta_t'^2, \left(\int_0^{a_{e_1}} \eta_t'^2 \right)^{\alpha_3}, \left(\int_{a_{e_2}}^S \eta_t'^2 \right)^{\alpha_4}, \left(\frac{1}{SN} \right)^{\alpha_5} \right],$$

and the mixed term $M(\eta_t, \mathbf{a}_c, \mathbf{a}_e, S, N, \boldsymbol{\alpha})$:

$$M(\eta_t, \mathbf{a}_c, \mathbf{a}_e, S, N, \boldsymbol{\alpha}) := \left[\left(\frac{\int_{a_{e_2}}^S \eta_t'^2}{\int_0^{a_{c_1}} \eta_t} \right)^{\alpha_6}, \left(\frac{\int_{a_{e_2}}^S \eta_t'^2}{\int_{a_{c_2}}^S \eta_t} \right)^{\alpha_7}, \left(\frac{N \int_{a_{e_2}}^S \eta_t'^2}{\int_0^{a_{c_1}} \eta_t} \right)^{\alpha_8}, \left(\frac{N \int_{a_{e_2}}^S \eta_t'^2}{\int_{a_{c_2}}^S \eta_t} \right)^{\alpha_9} \right].$$

We then combine these terms to define the optimization-feature vector for Opt-Laws:

$$F(\eta_t, \mathbf{a}_c, \mathbf{a}_e, S, N, \boldsymbol{\alpha}) := [C(\eta_t), M(\eta_t), N^{-\alpha_{10}}, S^{-\alpha_{11}}, \eta_{\max}^{\alpha_{12}}, 1], \quad (7)$$

where, for the sake of notation, we omit certain arguments of $C(\cdot)$, $E(\cdot)$, and $M(\cdot)$.

Discussion The optimization-feature vector $F(\cdot)$ is a 16-dimensional representation that captures key aspects of training dynamics. Although $F(\cdot)$ may seem complex, it is systematically constructed from theoretically grounded basis functions through multiplication and exponentiation. These functions capture essential elements of the training process, such as the convergence characteristics of the optimization and the model’s ability to escape local minima. For instance, the convergence terms $C(\cdot)$ suggest that maintaining a higher LR allows for a larger $\int \eta_t$, which accelerates the convergence. However, an excessively high LR can lead to increased $(\eta'_t)^2$ during warmup and cooldown, causing the escape terms $E(\cdot)$ to rise and potentially trapping the model in poor local minima. Unlike in Sec. 3.1, where model size was not factored in, introducing model size reveals a trade-off: larger models slow convergence (as $N/\int \eta_t$ increases) but reduce the escape terms (as $1/SN$ decreases), highlighting the need for balance. Additionally, the mixed terms provide insights into the interaction between model size and peak LR. For example, the term $N \int (\eta'_t)^2 / \int \eta_t$ indicates that when data size increases modestly while model size N grows significantly, reducing the peak LR becomes necessary to keep this term small. This aligns with empirical observations that the optimal peak LR tends to decrease as model size increases (Dubey et al., 2024).

Our feature vector $F(\cdot)$ contains sufficient information to model the relationship between training hyper-parameters and final loss, enabling us to derive generalized Opt-Laws through linear regression.

$$\log(\text{Loss}) = \mathbf{c}^\top F(\eta_t, \mathbf{a}_c, \mathbf{a}_e, S, N, \boldsymbol{\alpha}), \quad (\text{Opt-Laws})$$

where $(\eta_t, \mathbf{a}_c, \mathbf{a}_e, S, N)$ is the combination of training parameters, $\boldsymbol{\alpha}$ represents the powers of the basis functions, and \mathbf{c} is the solution to the following linear regression problem:

$$\mathbf{c} = \underset{\mathbf{c}}{\text{argmin}} \left\{ \sum_i \left(\mathbf{c}^\top F(\eta_t^i, \mathbf{a}_c^i, \mathbf{a}_e^i, S^i, N^i, \boldsymbol{\alpha}) - \log(\text{Loss}_i) \right)^2 \right\}, \quad (8)$$

where $(\eta_t^i, \mathbf{a}_c^i, \mathbf{a}_e^i, S^i, N^i)$ represents the different hyper-parameter combinations shown in Fig. 2, and Loss_i denotes the final training loss associated with each combination (excluding divergent losses during regression). Analogous to scaling laws, the exponents’ vector $\boldsymbol{\alpha}$ is a critical parameter. However, fitting $\boldsymbol{\alpha}$ alongside \mathbf{c} introduces significant non-convexity and non-smoothness into the regression problem, often rendering standard solvers inadequate. Therefore, $\boldsymbol{\alpha}$ is preselected based on intermediate cross-validation results during \mathbf{c} optimization. Despite not being directly optimized, this approach still ensures that the regression error remains low. The fitted \mathbf{c} and preselected $\boldsymbol{\alpha}$ values are detailed in Appendix Sec. A.

The proposed **Opt-Laws** can, under certain conditions, recover classical scaling laws. For instance, when the LR schedule is fixed and model size N is the only variable, normalizing N to a range much smaller than 1 allows **Opt-Laws** to approximate the broken neural scaling laws (BNSL) (Caballero et al., 2023). Specifically, BNSL is expressed as $\log(\text{Loss}) = \bar{b} + \sum_i \bar{c}_i \log(1 + N^{\bar{\alpha}_i}) \approx \bar{b} + \sum_i \bar{c}_i N^{\bar{\alpha}_i}$, where $\bar{\alpha}_i$ and \bar{b} are data-driven parameters and the approximation represents **Opt-Laws**. BNSL has been shown to outperform the classical Kaplan scaling laws across both upstream and downstream tasks. Furthermore, by applying a logarithmic transformation to N during normalization and selecting $\alpha_1 = \alpha_8 = \alpha_9 = \alpha_{10} = 1$, **Opt-Laws** can closely approximate the classical Kaplan and Chinchilla scaling laws (Kaplan et al., 2020; Hoffmann et al., 2022).

4.3 Applying Generalized Opt-Laws

In this section, we apply the generalized **Opt-Laws** to predict training loss and discuss the key parameters \mathbf{a}_c and \mathbf{a}_e .

The parameters \mathbf{a}_c and \mathbf{a}_e are essential for dividing LR schedules into multiple phases, allowing us to focus on the phases that have the most significant impact on the final loss. To illustrate our approach, we refer to a general LR schedule shown in Fig. 4. This schedule is broadly applicable, consisting of four distinct phases: an initial warmup, a subsequent decay, a plateau phase with constant LR, and a final cooldown. By dividing the schedule in this manner and considering the monotonicity within each phase, this general LR schedule can effectively represent various commonly used LR schedules in LLM training. For example, in cases involving a linear warmup followed by cosine decay (Gupta et al., 2023), one can set $a_1 = a_2 = a_3$ and allow the cooldown phase to follow a cosine curve. Similarly, recently proposed schedules like Constant LR with Cooldown (Hägele et al., 2024) can be treated as a special case where $a_1 = a_2 < a_3$, while more complex schedules, such as Infinite Learning Rate Schedules (Ibrahim et al., 2024), correspond to cases where $a_1 < a_2 < a_3$.

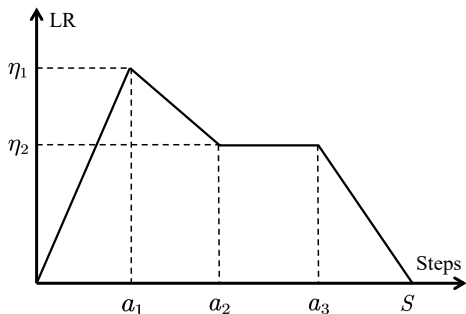


Figure 4: Illustration of a typical LR schedule comprising four phases: warmup, decay, plateau, and cooldown. This framework encompasses most LR schedules used in LLM training as special cases. We use this example to demonstrate the selection of the hyper-parameters \mathbf{a}_c and \mathbf{a}_e in **Opt-Laws**.

$a_1 = a_2 = a_3$ in Fig. 4). The right grid depicts the loss predictions generated by the generalized **Opt-Laws**. We used two-thirds of the data points for linear regression and reserved the remaining one-third for validation. The validation results show that the relative error between predicted and actual losses is within 0.5%.

Moreover, by leveraging the criterion $R(\eta_{\max}, a_1, N, S)$ from Eqn. (4), we can reliably identify hyper-parameter configurations that are likely to cause training divergence. The

For the convergence component in **Opt-Laws**, based on the LR schedule in Fig. 4, we set $a_{c_1} = a_1$ to represent the end of the warmup phase and $a_{c_2} = a_3$ to correspond to the start of the cooldown phase. We omit the segment between a_1 and a_3 from **Opt-Laws** as empirical results show that this phase has negligible impact on final loss fitting for our model and dataset. For the escape dynamics in **Opt-Laws**, we set $a_{e_1} = a_{e_2} = a_2$, focusing on the final non-increasing phase of the LR schedule to calculate the escape probability.

The parameters \mathbf{a}_c and \mathbf{a}_e discussed above are specifically tailored to our models and datasets. When applying the generalized **Opt-Laws** in different contexts, these parameters should be adjusted based on the specific loss data. Once properly calibrated, generalized **Opt-Laws** can effectively predict loss across various hyper-parameter configurations. Fig. 5 presents the results on small-scale models and datasets. For larger models (e.g., over 4B parameters trained on more than 300B tokens), refer to Sec. 6. In Fig. 5, the left grid shows the actual training outcomes under a linear warmup and cooldown LR schedule (where

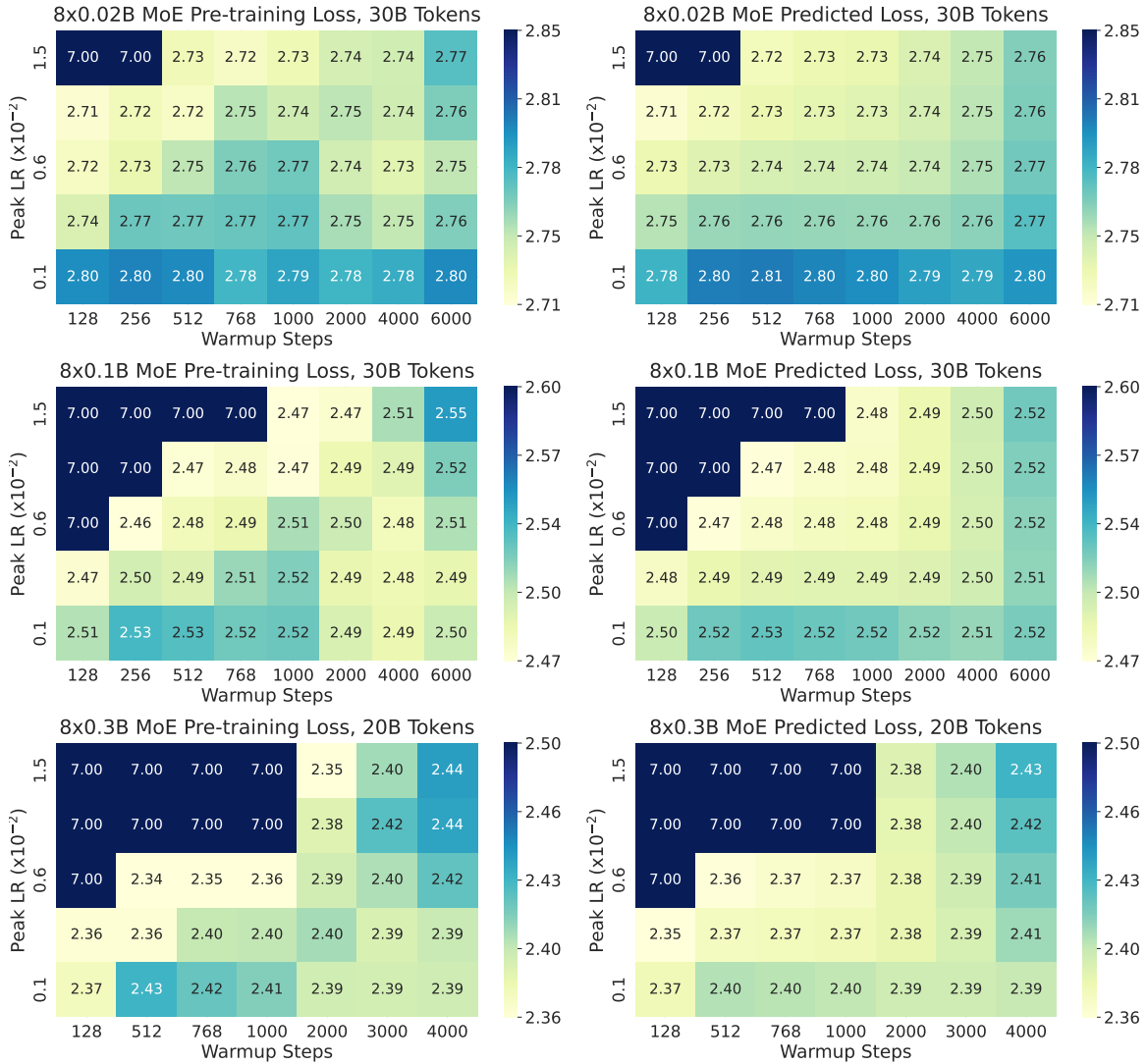


Figure 5: Comparison of actual training outcomes (left) and loss predictions generated by **Opt-Laws** (right) for a common LR schedule pattern with linear warmup and cooldown. In regions where $R(\eta_{\max}, a_1, N, S) > 1$, the divergence indicator from Eqn. (4), the predicted loss is set to 7 to signify training failure. The average relative error between the predicted and actual losses is within 0.5%, demonstrating the accuracy of **Opt-Laws**

generalized **Opt-Laws** also effectively capture the multi-modal nature of the loss landscape w.r.t. hyper-parameters, successfully identifying regions associated with higher loss, such as those observed in the $8 \times 0.1\text{B}$ and $8 \times 0.3\text{B}$ MoE settings. Notably, generalized **Opt-Laws** accurately identifies the hyper-parameter configurations corresponding to the regions with the lowest loss, which are often of greatest concern during LLM training. These findings, along with the results for larger models presented in Table 1, robustly validate the effectiveness and practical utility of the generalized **Opt-Laws**.

5 SDEs behind Opt-Laws

In this section, we derive Opt-Laws by analyzing the training dynamics of non-convex smooth optimization problems, specifically focusing on SGD and Adam (Kingma and Ba, 2014). We model these dynamics using SDEs, which is essential for capturing the effects of time-varying learning rates, especially complex schedules like cosine cooldowns that are challenging to analyze in discrete time.

Our analysis examines the influence of key hyper-parameters, including the LR schedule $\eta(t)$, data size D , and model size N , on two critical aspects: convergence speed and the ability to escape suboptimal local minima. Notably, we observe that both SGD and Adam yield similar forms in their bounds related to these hyper-parameters. This similarity allows us to generalize Opt-Laws, encapsulating the relationship between these factors and the final training loss, thereby offering deeper insights into the optimization process.

While existing research frequently uses SDEs to model optimization processes and analyze convergence (Li et al., 2017; Soto et al., 2022; Dambrine et al., 2024), or to study escape time from local minima (e.g., the Eyring–Kramers law (Berglund and Gentz, 2013; Bovier and Den Hollander, 2015)), these studies are predominantly restricted to convex problems, quadratic objectives, or fixed learning rates. In contrast, our work extends to general non-convex smooth problems with time-varying LRs, thus leading to a nonlinear, time-inhomogeneous SDE. This added complexity precludes the direct application of existing results. Our contributions address these new theoretical challenges, providing novel insights into the optimization of LLMs under more general conditions.

5.1 Optimization Methods and SDEs

We study the following non-convex optimization problem:

$$\min_{\mathbf{x}} f(\mathbf{x}) := \mathbb{E}_{\zeta \sim \mathcal{D}}[F(\mathbf{x}, \zeta)], \quad (9)$$

where the objective function $F(\cdot, \cdot)$ is differentiable and possibly non-convex, data ζ is drawn from an unknown data distribution \mathcal{D} , \mathbf{x} is the learnable parameters. The formulation Eqn. (9) encapsulates a large body of machine learning problems, e.g., LLM training problems, and least square regression. For SGD, the update scheme is as follows:

$$\mathbf{x}_{k+1} = \mathbf{x}_k - \eta_0 \eta_k \tilde{\mathbf{g}}_k, \quad (\text{SGD})$$

where gradient estimate $\tilde{\mathbf{g}}_k$ is defined as $\tilde{\mathbf{g}}_k := \nabla f(\mathbf{x}_k) + \mathbf{z}_k$, with a LR of $\eta_0 \eta_k$, where η_0 is a small rescaling parameter and η_k is the normalized LR. This choice of LR facilitates the derivation of the corresponding SDE. Following previous work (Zhu et al., 2019; Malladi et al., 2022; Xie et al., 2020; Zhou et al., 2024b), we assume $\mathbf{z}_k \sim \mathcal{N}(0, \Sigma(\mathbf{x}_k))$, where

$$\Sigma(\mathbf{x}_k) := \frac{1}{B} \left(\frac{1}{D} \sum_{i=1}^D (\nabla F(\mathbf{x}_k, \zeta_i) - \nabla f(\mathbf{x}_k)) (\nabla F(\mathbf{x}_k, \zeta_i) - \nabla f(\mathbf{x}_k))^\top \right). \quad (10)$$

The exact characterization of the noise \mathbf{z}_k in stochastic optimization remains unresolved (Simsekli et al., 2019; Zhang et al., 2021). For analytical convenience, we adopt a Gaussian

noise assumption, acknowledging that determining the precise stochastic process of the noise during LLM training is beyond this work’s scope.

Under mild conditions, SGD can be approximated by an Itô-SDE, where the noise is modeled by Brownian motion, as derived via the Euler-Maruyama method in Sec. B.2:

$$d\mathbf{X}_t = -\eta(t)\nabla f(\mathbf{X}_t)dt + \sqrt{\eta_0}\eta(t)\sigma(\mathbf{X}_t)d\mathbf{W}_t. \quad (\text{SGD-SDE})$$

where \mathbf{W}_t is a Wiener process, $\sigma : \mathbb{R}^N \rightarrow \mathbb{R}^{N \times N}$ is defined as $\sigma(\mathbf{x}) := \sqrt{\Sigma(\mathbf{x})}$, $\eta(t)$ is the normalized LR schedule, and η_0 is a small rescaling parameter. Specifically, $\eta_0 \cdot \eta(t)$ corresponds to the original LR schedule.

Similarly, the dynamics of the Adam can be approximated using a lifted Itô-SDE. The algorithmic steps for Adam are presented as follows:

$$\begin{cases} \mathbf{x}_{k+1} = \mathbf{x}_k - \eta_0\eta_k\mathbf{m}_k \odot (\mathbf{v}_k + \epsilon)^{-\frac{1}{2}}, \\ \mathbf{m}_{k+1} = (1 - \beta_{1,k})\mathbf{m}_k + \beta_{1,k}\tilde{\mathbf{g}}_{k+1}, \\ \mathbf{v}_{k+1} = (1 - \beta_{2,k})\mathbf{v}_k + \beta_{2,k}\tilde{\mathbf{g}}_{k+1}^2, \end{cases} \quad (\text{Adam})$$

where \odot denotes the element-wise product, with $\beta_{1,k}, \beta_{2,k} \in (0, 1)$ and initial conditions $\mathbf{m}_0 = \mathbf{v}_0 = \mathbf{0}$. The parameter ϵ prevents degeneracy. In practice, both $\beta_{1,k}$ and $\beta_{2,k}$ are typically close to 1. To facilitate SDE-based analysis, we use the parameters $\beta_{1,k} = 1 - \hat{c}_1\eta_k$ and $\beta_{2,k} = 1 - \hat{c}_2\eta_k$, following a single-time scale scheme (Ding et al., 2023; Shen and Chen, 2022; Xiao et al., 2023), where \hat{c}_1 and \hat{c}_2 are small constants. The resulting Itô-SDE for Adam’s dynamics is:

$$\begin{cases} d\mathbf{X}_t = -\eta(t)\mathbf{m}_t \odot (\mathbf{v}_t + \epsilon)^{-\frac{1}{2}}dt, \\ d\mathbf{m}_t = -c_1\eta(t)(\mathbf{m}_t - \nabla f(\mathbf{X}_t))dt + c'_1\eta(t)\sigma(\mathbf{X}_t)d\mathbf{W}_t, \\ d\mathbf{v}_t = -c_2\eta(t)(\mathbf{v}_t - \text{diag}(\Sigma(\mathbf{X}_t)))dt, \end{cases} \quad (\text{Adam-SDE})$$

where c_1, c'_1 , and c_2 are constants. The notation $\text{diag}(\mathbf{M})$ refers to the vector formed by the diagonal elements of matrix \mathbf{M} , while $\text{Diag}(\mathbf{v})$ denotes the diagonal matrix with the entries of \mathbf{v} on its diagonal. Given the initial condition $\mathbf{v}_0 = \mathbf{0}$, the solution for \mathbf{v}_t is:

$$\mathbf{v}_t = \exp\left(-c_2 \int_0^t \eta(s)ds\right) \left[\int_0^t \exp\left(c_2 \int_0^s \eta(\tau)d\tau\right) c_2\eta(s)\mathbf{d}_s ds \right],$$

where $\mathbf{d}_t := \text{diag}(\Sigma(\mathbf{X}_t))$. This formulation ensures that \mathbf{v}_t remains nonnegative throughout the process.

5.2 Inspiration from Convergence Guarantee

In this subsection, we analyze the convergence properties of (SGD-SDE) and (Adam-SDE) in the context of non-convex smooth problems, deriving the mathematical formula for the convergence component of Opt-Laws. To present these results rigorously, we first provide several mild assumptions. In the following discussion, the notation $\|\cdot\|$ denotes the Euclidean norm when applied to vectors and the Frobenius norm when applied to matrices. While $\|\cdot\|_{\text{op}}$ denotes the operator norm for matrix.

Assumption 1 (L-smoothness) *The function $f(\cdot)$ is L -smooth with respect to the parameters, namely,*

$$\|\nabla f(\mathbf{x}) - \nabla f(\mathbf{y})\| \leq L\|\mathbf{x} - \mathbf{y}\|, \quad \forall \mathbf{x}, \mathbf{y} \in \mathbb{R}^N.$$

Assumption 2 (Unbiased Estimator) *Given any $\mathbf{x} \in \mathbb{R}^N$, we assume that the entries of $\nabla F(\mathbf{x}, \zeta_i) - \nabla f(\mathbf{x})$ are i.i.d. Gaussians $\mathcal{N}(0, \Sigma_g)$ for all $i \in [D]$, where Σ_g is given.*

Assumption 1 asserts that the objective function of our optimization problem is L -smooth. This is a standard and mild assumption in the stochastic optimization literature, which facilitates the determination of specific convergence rates for optimization algorithms, a task that is otherwise challenging (Arjevani et al., 2022; Guo et al., 2021; Li and Lin, 2022; Xie et al., 2022, 2024b,a; Zhou et al., 2024a). Assumption 2 stipulates that the noise introduced by different data points during the estimation of the gradient is unbiased and independent, given the weights of LLMs. This assumption is also common, especially when the Langevin diffusion is employed to analyze the behavior of SGD (Jastrzębski et al., 2017; He et al., 2019; Xie et al., 2020). Notably, we do not assume that the gradient estimation noise originates from an oracle distribution $\mathcal{N}(0, \Sigma)$. As indicated in Eqn. (10), the covariance matrix encountered during actual training is not $\mathbb{E}_{\zeta \sim \mathcal{D}}[(\nabla F(\mathbf{x}, \zeta_i) - \nabla f(\mathbf{x}))(\nabla F(\mathbf{x}, \zeta_j) - \nabla f(\mathbf{x}))^\top]$.

Under these assumptions, we derive a concentration inequality for the trace of the covariance matrix $\Sigma(\mathbf{x}_k)$ defined in Eqn. (10), which is helpful for the following analysis. In this work, the batch size B is fixed. For simplicity, we assume $B = 1$ throughout the analysis. However, the results are readily adaptable to any fixed positive batch size B .

Proposition 2 (Trace Boundedness) *Suppose Assumption 2 holds. Given any point $\mathbf{x} \in \mathbb{R}^N$ and a positive $t > 0$, the covariance matrix in Eqn. (10) satisfies*

$$\mathbb{P}\left(|\text{Tr}(\Sigma(\mathbf{x})) - \text{Tr}(\Sigma_g)| \geq t\right) \leq 2 \exp\left(-\frac{Dt^2}{4\text{Tr}(\Sigma_g^2) + 2t\sigma_g^2}\right),$$

where D is the number of samples and $\sigma_g := \lambda_{\max}\left(\Sigma_g^{\frac{1}{2}}\right)$ is the largest eigenvalue of $\Sigma_g^{\frac{1}{2}}$.

We can also estimate the maximal eigenvalue of the random matrix $\Sigma(\mathbf{x})$ by random matrix theory.

Proposition 3 (Covariance Boundedness) *Suppose Assumption 2 holds, then the covariance matrix in Eqn. (10) satisfies*

$$\sup_{\mathbf{x} \in \mathbb{R}^N} \mathbb{E}[\lambda_{\max}(\Sigma(\mathbf{x}))] \leq \left(1 + \sqrt{\frac{D}{N}}\right) \sigma_g^2 + \frac{C\sigma_g^2}{N^{2/3}}.$$

where $C > 0$ is a constant independent of N , the expectation is taken with respect to the Gaussian distribution $\mathcal{N}(0, \Sigma_g)$ specified in Assumption 2, and $\sigma_g := \lambda_{\max}\left(\Sigma_g^{\frac{1}{2}}\right)$.

Proposition 3 provides a non-asymptotic extension of the classical Marchenko-Pastur theorem (Bai and Silverstein, 2010; Ledoux and Rider, 2010) from random matrix theory, offering a more precise variance estimate based on the convergence of the largest eigenvalue of covariance matrices to $(1 + \sqrt{D/N})\sigma_g^2$. For most LLMs adhering to scaling laws, the ratio $D/N \gg 1$. Consequently, we can expect $\lambda_{\max}(\Sigma(\mathbf{x})) = \mathcal{O}\left(\sigma_g^2 \sqrt{D/N}\right)$ in expectation.

5.2.1 SGD CONVERGENCE ANALYSIS

With the smoothness and boundedness properties established, we can now derive the expected convergence rate of SGD-SDE for non-convex problems in terms of time-varying LRs.

Theorem 1 (SGD Convergence Bound) *Suppose Assumptions 1 and 2 hold. For the dynamics described in (SGD-SDE), the following bound holds:*

$$\mathbb{E} \left[\overline{\|\nabla f(\mathbf{X}_t)\|^2} \right] \leq \frac{f(\mathbf{X}_0) - f_{\min}}{\int_0^t \eta(s) ds} + \frac{\eta_0 L \sigma_0^2 N \int_0^t \eta(s)^2 ds}{2 \int_0^t \eta(s) ds}, \quad (11)$$

where $\overline{\|\nabla f(\mathbf{X}_t)\|^2} := \frac{\int_0^t \eta(s) \|\nabla f(\mathbf{X}_s)\|^2 ds}{\int_0^t \eta(s) ds}$ and $f_{\min} := \min_{\mathbf{x} \in \mathbb{R}^N} f(\mathbf{x})$, and

$$\sigma_0 := \sigma_g \sqrt{\left(1 + \sqrt{\frac{D}{N}}\right) + \frac{C}{N^{\frac{2}{3}}}}.$$

It can be observed that the average squared norm of the gradient can be effectively upper bounded by a function of the training hyper-parameters. Given a maximal time horizon $T > 0$, the bound in Eqn. (11) achieves the optimal bound of $\mathcal{O}(1/\sqrt{T})$ when we select constant LR $\eta(t) = \mathcal{O}(1/\sqrt{T})$. This upper bound consists of two terms, both of which share the denominator of $\int_0^t \eta(s) ds$. Despite the complexity inherent in the numerator, the numerator of the first term is clearly of the order $\mathcal{O}(N)$, given that $f(\mathbf{X}_0) - f_{\min} \leq \frac{L}{2} \|\mathbf{X}_0 - \mathbf{X}^*\|^2$, where $\mathbf{X}^* \in \arg\min_{\mathbf{x}} f(\mathbf{x})$. The magnitude of the numerator in the second term is also $\mathcal{O}(N)$. Thus, the overall order of the average squared norm of the gradient is $\mathcal{O}(N/\int_0^t \eta(s) ds)$.

5.2.2 ADAM CONVERGENCE ANALYSIS

We proceed to analyze the convergence of (Adam-SDE). Before delving into this analysis, we need to introduce an additional mild assumption, which is commonly employed in the study of stochastic first-order methods (Bertsekas and Tsitsiklis, 2000; Reddi et al., 2018).

Assumption 3 (Smoothness and Boundedness) *The function $f(\cdot)$ is smooth with respect to the parameters and the normalized LR schedule is bounded,*

1. $|f(\mathbf{x}) - f(\mathbf{y})| \leq \ell \|\mathbf{x} - \mathbf{y}\| \quad \forall \mathbf{x}, \mathbf{y} \in \mathbb{R}^N$,
2. $\int_0^\infty \eta(s) ds = \infty, \quad \int_0^\infty \eta^2(s) ds < \infty$.

Assumption 3.1 asserts global Lipschitz continuity, implying that the gradient of f is uniformly bounded. This is a common assumption in extensive literature on adaptive gradient methods (Reddi et al., 2018; Xiao et al., 2024; Xie et al., 2024b). Assumption 3.2 requires that the LR be non-summable but square summable, which is a fundamental assumption for ensuring the convergence of stochastic first-order methods (Bertsekas and Tsitsiklis, 2000; Davis et al., 2020). Based on this assumption, we first establish the boundedness of the (Adam-SDE) dynamics as follows. The boundedness helps to guarantee the convergence of (Adam-SDE). From Proposition 3, we can observe that the maximal eigenvalue of $\Sigma(\mathbf{x})$ can be bounded by $\mathcal{O}\left(\sigma_g^2 \sqrt{D/N}\right)$ in expectation. Based on this observation, we make the following stronger assumption than Assumption 2 to establish the convergence of Adam.

Assumption 4 *There exists $\bar{\sigma}$, such that $\lambda_{\max}(\Sigma(\mathbf{x})) \leq \bar{\sigma}$ for all $\mathbf{x} \in \mathbb{R}^N$.*

Proposition 4 (Dynamics Boundedness) *Suppose Assumptions 3 and 4 hold, then there exist positive constants M and V which are independent of N , such that*

$$\sup_{t \geq 0} \left\{ \mathbb{E} \left[\|\mathbf{m}_t\|^2 \right] \right\} \leq M^2 N, \quad \sup_{t \geq 0} \{\|\mathbf{v}_t\|_\infty\} \leq V.$$

This proposition demonstrates uniform bounds for \mathbf{m}_t and \mathbf{v}_t . The distinction is that the bound for \mathbf{v}_t is deterministic, whereas the bound for \mathbf{m}_t is in the sense of expectation. This is due to the SDE associated with \mathbf{m}_t involving a Brownian motion. Since both M and V are independent of N , the scales of \mathbf{m}_t and \mathbf{v}_t are matched in the sense that both $\mathbb{E}[\|\mathbf{m}_t\|^2]$ and $\mathbb{E}[\|\mathbf{v}_t\|^2]$ are of the order $\mathcal{O}(N)$.

Theorem 2 (Adam Convergence Bound) *Suppose Assumptions 1, 3 and 4 hold. For the dynamics of (Adam-SDE), the following bound holds:*

$$\mathbb{E} \left[\overline{\|\mathbf{m}_t\|^2} \right] \leq \frac{\sqrt{V+\epsilon} \left(f(\mathbf{X}_0) + \frac{1}{2c_1} \left\langle \frac{\mathbf{m}_0}{\sqrt{\mathbf{v}_0+\epsilon}}, \mathbf{m}_0 \right\rangle - f_{\min} \right) + \frac{(c'_1)^2 \bar{\sigma} \sqrt{V+\epsilon} \int_0^t \eta(s)^2 ds}{2c_1}}{\left(1 - \frac{c_2}{4c_1} \right) \int_0^t \eta(s) ds} + \frac{\frac{(c'_1)^2 \bar{\sigma} \sqrt{V+\epsilon} \int_0^t \eta(s)^2 ds}{2c_1}}{\left(1 - \frac{c_2}{4c_1} \right) \sqrt{\epsilon} \int_0^t \eta(s) ds}, \quad (12)$$

where $\overline{\|\mathbf{m}_t\|^2} := \frac{\int_0^t \eta(s) \|\mathbf{m}_s\|^2 ds}{\int_0^t \eta(s) ds}$, and $f_{\min} := \min_{\mathbf{x} \in \mathbb{R}^N} f(\mathbf{x})$. Moreover, we also have

$$\begin{aligned} \mathbb{E} \left[\overline{\|\nabla f(\mathbf{X}_t)\|^2} \right] &\leq \frac{2\sqrt{V+\epsilon} \left(f(\mathbf{X}_0) - \frac{1}{c_1} \left\langle \nabla f(\mathbf{X}_0), \frac{\mathbf{m}_0}{\sqrt{\mathbf{v}_0+\epsilon}} \right\rangle - f_{\min} + \frac{\ell M \sqrt{N}}{c_1 \sqrt{\epsilon}} \right)}{\int_0^t \eta(s) ds} \\ &\quad + \left(\frac{2L\sqrt{V+\epsilon}}{c_1 \epsilon} + \left(1 + \frac{\bar{\sigma}^2}{\epsilon^2} \right) \frac{c_2^2 (V+\epsilon)}{2c_1^2 \epsilon} \right) \mathbb{E} \left[\overline{\|\mathbf{m}_t\|^2} \right]. \end{aligned} \quad (13)$$

Theorem 2 outlines the convergence rates of the momentum \mathbf{m}_t and gradient $\nabla f(\mathbf{X}_t)$ in (Adam-SDE). When focusing solely on the LR schedule $\eta(t)$, and ignoring N and other Lipschitz constants, the bound for $\mathbb{E} \left[\overline{\|\mathbf{m}_t\|^2} \right]$ simplifies to $\mathcal{O} \left(\frac{1}{\int_0^t \eta(s) ds} + \frac{\int_0^t \eta(s)^2 ds}{\int_0^t \eta(s) ds} \right)$. By Eqn. (13), the bound for $\mathbb{E} \left[\overline{\|\nabla f(\mathbf{X}_t)\|^2} \right]$ is identical, indicating that $\mathbb{E} \left[\overline{\|\nabla f(\mathbf{X}_t)\|^2} \right]$ and $\mathbb{E} \left[\overline{\|\mathbf{m}_t\|^2} \right]$ share the same convergence rate in terms of $\eta(t)$.

Discussion Theorems 1 and 2 collectively demonstrate a common relationship between the optimization hyper-parameters and the gradient norm from an SDE perspective. Both theorems suggest that the average squared norm of the gradient can be upper bounded by $\mathcal{O}(N^\gamma / \int_0^t \eta(s) ds)$, where $\gamma \geq 1$ is a constant. It is important to note that the magnitude of $f(\mathbf{x}_t) - f(\mathbf{x}^*)$ is positively correlated with the gradient norm in smooth cases, where \mathbf{x}^* is a local minimum in the current region. Consequently, the relationship between the training loss and the hyper-parameters $\eta(t)$ can also be expressed as $c(N / \int_0^t \eta(s) ds)^\alpha$.

As in Opt-Laws, we introduce the constants c and α to generalize the relationship between convergence rate and training loss. These parameters are essential because $\mathcal{O}(N^\gamma / \int_0^t \eta(s) ds)$ reflects the worst-case convergence rate, while the actual rate depends on the specific architectures of LLMs, data, and training techniques. Therefore, a data-driven approach is used to determine c and α , ensuring these parameters are more practically applicable, as worst-case bounds are often too conservative for LLM training strategies.

5.3 Inspiration from Escaping Capacity

Effective optimization hyper-parameters can expedite escaping sharp local minima during training, which is why large LRs are favored when training LLMs, followed by cooldown techniques. These strategies help LLMs efficiently move away from sharp local minima, enhancing overall generalization performance. Building on this idea, this subsection quantitatively investigates the escape capacity of (SGD-SDE) and (Adam-SDE). We calculate the probability of these dynamics escaping a local region, providing a rigorous analysis of their effectiveness in avoiding suboptimal solutions.

5.3.1 LINEARIZATION APPROXIMATION OF SDES

In the context of SDEs, the density of the solutions adheres to the Fokker-Planck-Kolmogorov (FPK) equation. For instance, in the case of (SGD-SDE), the specific FPK form is

$$\frac{\partial p(\mathbf{x}, t)}{\partial t} = \sum_{i=1}^N \frac{\partial}{\partial x_i} [\eta(t) \nabla_i f(\mathbf{x}) p(\mathbf{x}, t)] + \frac{\eta_0}{2} \sum_{i,j} \frac{\partial^2}{\partial x_i \partial x_j} [\Sigma(\mathbf{x})_{ij} \eta^2(t) p(\mathbf{x}, t)], \quad (14)$$

where $p(\mathbf{x}, t)$ denotes the density of \mathbf{X}_t at time t , $\Sigma(\mathbf{x})_{ij}$ is the (i, j) -th entry of the covariance matrix $\Sigma(\mathbf{x})$ in Eqn. (10), $\nabla_i f(\mathbf{x})$ is the i -th component of the gradient $\nabla f(\mathbf{x})$, and the initial distribution is specified by the Dirac delta function $\delta(\mathbf{x} - \mathbf{X}_0)$. The non-linearity and time-dependent nature of the FPK equation pose significant challenges for deriving analytical solutions. Consequently, it is difficult to directly estimate the exit times using the density function $p(\mathbf{x}, t)$. A common approach is to approximate the operators in Eqn. (14), to make the estimation of exit times more tractable.

Given the density $p(\mathbf{x}, t)$ at time t , we aim to determine the density $p(\mathbf{x}, t + \Delta_t)$ at time $t + \Delta_t$. Note that the transition density over the interval $[t, t + \Delta_t]$ still satisfies Eqn. (14) with the initial condition $p(\mathbf{x}, t)$. We then perform a local linear approximation of Eqn. (14), for all $s \in [t, t + \Delta_t]$:

$$\begin{aligned} \frac{\partial p(\mathbf{x}, s)}{\partial s} &\approx \sum_{i=1}^N \frac{\partial}{\partial x_i} \left\{ \eta(s) p(\mathbf{x}, s) \nabla_i f(\bar{\mathbf{x}}_t) + \eta(s) p(\mathbf{x}, s) [\nabla^2 f(\bar{\mathbf{x}}_t)(\mathbf{x} - \bar{\mathbf{x}}_t)]_i \right\} \\ &+ \frac{\eta_0}{2} \sum_{i,j} \frac{\partial^2}{\partial x_i \partial x_j} [\eta^2(s) p(\mathbf{x}, s) \Sigma(\bar{\mathbf{x}}_t)_{ij}], \end{aligned} \quad (15)$$

where the drift term $\nabla f(\mathbf{x})$ is approximated by its first order expansion around the mean value $\bar{\mathbf{x}}_t := \mathbb{E}[\mathbf{X}_t]$ at time t , while the diffusion term $\Sigma(\mathbf{x})$ is approximated by its value at $\bar{\mathbf{x}}_t$ without expansion. Higher-order terms are neglected. This local linearization implies that the FPK equation now describes a local Ornstein-Uhlenbeck process. Consequently, the solution $p(\mathbf{x}, s)$ becomes a Gaussian distribution $\forall s \in [t, t + \Delta_t]$. By iteratively applying such local approximations and letting $\Delta_t \rightarrow 0$, the dynamics of \mathbf{X}_t evolve into a Gaussian process derived from piecewise linear approximations. The mean $\bar{\mathbf{x}}_t := \mathbb{E}[\mathbf{X}_t]$ and variance $\mathbf{P}_t := \text{Cov}(\mathbf{X}_t)$ of this process are governed by the ODEs as follows:

$$\begin{cases} \frac{d\bar{\mathbf{x}}_t}{dt} = -\eta(t) \nabla f(\bar{\mathbf{x}}_t), \\ \frac{d\mathbf{P}_t}{dt} = -\eta(t) \mathbf{P}_t \nabla^2 f(\bar{\mathbf{x}}_t) - \eta(t) \nabla^2 f(\bar{\mathbf{x}}_t) \mathbf{P}_t + \eta_0 \eta^2(t) \Sigma(\bar{\mathbf{x}}_t). \end{cases} \quad (\text{SDE-GA})$$

Since $\{\mathbf{X}_t\}$ is a Gaussian process, the solutions to the ODEs (**SDE-GA**) for the mean and variance fully determine the form of the density. This allows us to analytically determine $p(\mathbf{x}, t)$, which is pivotal for estimating the escape probability from a local region. These approximations, also known in the literature as Gaussian approximations (GAs) (Solin et al., 2021; Archambeau et al., 2007), are widely utilized in filtering theory (Särkkä and Sarmavuori, 2013; Särkkä et al., 2015). For a comprehensive overview, please refer to Särkkä and Solin (2019), Sec. 9.1.

5.3.2 ESCAPE PROBABILITY FROM LOCAL MINIMA

The GA results for both (**SGD-SDE**) and (**Adam-SDE**) are provided as follows:

Proposition 5 (SGD-SDE Approximation) *Considering any local minimum \mathbf{x}^* of $f(\cdot)$, and setting the initial conditions of (**SGD-SDE**) as $\mathbf{X}_0 = \mathbf{x}^*$ and $\mathbf{P}_0 = \mathbf{0}$, the mean $\bar{\mathbf{x}}_t := \mathbb{E}[\mathbf{X}_t]$ and variance $\mathbf{P}_t := \text{Cov}(\mathbf{X}_t)$ of the (**SDE-GA**) for (**SGD-SDE**) satisfies the following ODE:*

$$\begin{cases} \frac{d\bar{\mathbf{x}}_t}{dt} = \mathbf{0}, \\ \frac{d\mathbf{P}_t}{dt} = -\eta(t)\mathbf{P}_t\mathbf{H} - \eta(t)\mathbf{H}\mathbf{P}_t + \eta_0\eta^2(t)\boldsymbol{\Sigma}, \end{cases} \quad (16)$$

where $\mathbf{H} := \nabla^2 f(\mathbf{x}^*)$, and the definition of $\boldsymbol{\Sigma} := \boldsymbol{\Sigma}(\mathbf{x}^*)$ is provided in Eqn. (10). Furthermore, the solution to Eqn. (16) has the following closed form:

$$\mathbf{P}_t = \mathbf{A}(t) \left(\int_0^t \exp\left(\mathbf{H} \int_0^s \eta(\tau) d\tau\right) \boldsymbol{\Sigma} \exp\left(\mathbf{H} \int_0^s \eta(\tau) d\tau\right) \eta_0 \eta^2(s) ds \right) \mathbf{A}(t), \quad (17)$$

where

$$\mathbf{A}(t) = \exp\left(-\mathbf{H} \int_0^t \eta(s) ds\right).$$

We can reformulate the (**Adam-SDE**) in the similar form of (**SGD-SDE**). Let $\mathbf{Z}_t := [\mathbf{X}_t; \mathbf{m}_t; \mathbf{v}_t]$ and $\widehat{\mathbf{W}}_t$ be the $3N$ -dimensional Brownian motion. Then, (**Adam-SDE**) can be rewritten as

$$d\mathbf{Z}_t = -\eta(t) \underbrace{\begin{bmatrix} \mathbf{m}_t \odot (\mathbf{v}_t + \epsilon)^{-\frac{1}{2}} \\ c_1(\mathbf{m}_t - \nabla f(\mathbf{X}_t)) \\ c_2(\mathbf{v}_t - \text{diag}(\boldsymbol{\Sigma}(\mathbf{X}_t))) \end{bmatrix}}_{=: \mathbf{F}(\mathbf{Z}_t)} dt + c'_1 \eta(t) \begin{bmatrix} \mathbf{0} & & \\ & \sigma(\mathbf{X}_t) & \\ & & \mathbf{0} \end{bmatrix} d\widehat{\mathbf{W}}_t. \quad (18)$$

Subsequently, the Jacobian of $\mathbf{F}(\mathbf{Z})$ with respect to \mathbf{Z} is given by:

$$\partial_{\mathbf{Z}} \mathbf{F}(\mathbf{Z}) = \begin{bmatrix} \mathbf{0} & \text{Diag}(\mathbf{v} + \epsilon)^{-\frac{1}{2}} & -\frac{1}{2} \text{Diag}(\mathbf{m} \odot (\mathbf{v} + \epsilon)^{-\frac{3}{2}}) \\ -c_1 \nabla^2 f(\mathbf{X}) & c_1 \mathbf{I} & \mathbf{0} \\ -c_2 \partial_{\mathbf{X}} \text{diag}(\boldsymbol{\Sigma}(\mathbf{X})) & \mathbf{0} & c_2 \mathbf{I} \end{bmatrix}. \quad (19)$$

Based on the reformulation, we also have a similar GA approximation for (**Adam-SDE**).

Proposition 6 (Adam-SDE Approximation) Denote $\bar{\mathbf{z}}_t := \mathbb{E}[\mathbf{Z}_t]$ and $\hat{\mathbf{P}}_t := \text{Cov}(\mathbf{Z}_t)$. Consider any local minimum \mathbf{x}^* of $f(\cdot)$ and set the initial conditions of (Adam-SDE) as $\mathbf{X}_0 = \mathbf{x}^*$, $\mathbf{m}_0 = \mathbf{0}$, $\mathbf{v}_0 = \text{diag}(\boldsymbol{\Sigma}(\mathbf{x}^*))$ and $\mathbf{P}_0 = \mathbf{0}$. The Gaussian approximation for (Adam-SDE) satisfies

$$\begin{cases} \frac{d\bar{\mathbf{z}}_t}{dt} = \mathbf{0}, \\ \frac{d\hat{\mathbf{P}}_t}{dt} = -\eta(t)\hat{\mathbf{P}}_t\hat{\mathbf{H}}^\top - \eta(t)\hat{\mathbf{H}}\hat{\mathbf{P}}_t + (c'_1)^2\eta(t)^2\hat{\boldsymbol{\Sigma}}, \end{cases} \quad (20)$$

where

$$\hat{\mathbf{H}} := \begin{bmatrix} \mathbf{0} & \text{Diag}(\boldsymbol{\Sigma}(\mathbf{x}^*) + \epsilon\mathbf{I})^{-\frac{1}{2}} & \mathbf{0} \\ -c_1\nabla^2 f(\mathbf{x}^*) & c_1\mathbf{I} & \mathbf{0} \\ -c_2\partial_{\mathbf{X}}\text{diag}(\boldsymbol{\Sigma}(\mathbf{x}^*)) & \mathbf{0} & c_2\mathbf{I} \end{bmatrix}, \quad \text{and} \quad \hat{\boldsymbol{\Sigma}} := \begin{bmatrix} \mathbf{0} & & \\ & \boldsymbol{\Sigma}(\mathbf{x}^*) & \\ & & \mathbf{0} \end{bmatrix}.$$

Furthermore, the solution to Eqn. (20) has the following closed form:

$$\hat{\mathbf{P}}_t = \hat{\mathbf{A}}(t) \left(\int_0^t \exp\left(\hat{\mathbf{H}} \int_0^s \eta(\tau) d\tau\right) \hat{\boldsymbol{\Sigma}} \exp\left(\hat{\mathbf{H}}^\top \int_0^s \eta(\tau) d\tau\right) (c'_1)^2 \eta(s)^2 ds \right) \hat{\mathbf{A}}^\top(t), \quad (21)$$

where

$$\hat{\mathbf{A}}(t) = \exp\left(-\hat{\mathbf{H}} \int_0^t \eta(s) ds\right).$$

Propositions 5 and 6 indicate that, under specified initial conditions, the approximated solutions to both (SGD-SDE) and (Adam-SDE) follow Gaussian distribution with mean \mathbf{x}^* . For ease of notation, we will continue to denote this Gaussian approximated solution as \mathbf{X}_t throughout this paper. By leveraging the anti-concentration inequality (Carbery and Wright, 2001), we can effectively calculate the probability that \mathbf{X}_T remains within the local vicinity of \mathbf{x}^* after a time period T . A smaller probability suggests a greater likelihood of escape from this region, indicating better escape capacity.

Theorem 3 (SGD Escape Probability) With the same initial conditions specified in Propositions 5, the Gaussian approximated solution for (SGD-SDE) satisfies

$$\mathbb{P}[\|\mathbf{X}_t - \mathbf{x}^*\|^2 \geq \epsilon] \geq 1 - \sqrt{\frac{e\epsilon}{\text{Tr}(\mathbf{P}_t)}},$$

where \mathbf{P}_t is the covariance matrix of \mathbf{X}_t defined in Eqn. (17). Suppose Assumption 2 holds, and considering the learning rate conditions $\eta(0) = \eta_{\max}$ and $\eta(T) = 0$, then we have

$$\mathbb{P}[\|\mathbf{X}_T - \mathbf{x}^*\|^2 \leq \epsilon] = \mathcal{O}\left(\left(\frac{\epsilon}{\eta_{\max}^4 \text{Tr}(\boldsymbol{\Sigma}_g)} \int_0^T \eta'(s)^2 ds\right)^{1/2}\right).$$

Theorem 4 (Adam Escape Probability) With the same initial conditions specified in Propositions 6, the Gaussian approximated solution for (Adam-SDE) satisfies

$$\mathbb{P}[\|\mathbf{X}_t - \mathbf{x}^*\|^2 \geq \epsilon] \geq 1 - \sqrt{\frac{e\epsilon}{\text{Tr}(\hat{\mathbf{P}}_t)}},$$

where $\widehat{\mathbf{P}}_t$ is the covariance matrix of \mathbf{Z}_t defined in Eqn. (21). Suppose Assumption 2 holds, and considering the learning rate conditions $\eta(0) = \eta_{\max}$ and $\eta(T) = 0$, then we have

$$\mathbb{P}[\|\mathbf{X}_T - \mathbf{x}^*\|^2 \leq \varepsilon] = \mathcal{O}\left(\left(\frac{\varepsilon}{\eta_{\max}^4 \text{Tr}(\boldsymbol{\Sigma}_g)} \int_0^T \eta'(s)^2 ds\right)^{1/2}\right).$$

Theorems 3 and 4 provide lower bounds on the probability that \mathbf{X}_t is located outside an ε -radius ball centered in \mathbf{x}^* after time t . A larger lower bound indicates a stronger escaping capacity of \mathbf{X}_t . Equivalently, a smaller probability that \mathbf{X}_T remains within the local region of \mathbf{x}^* after the LR has cooled down (at time T) suggests a greater capacity of \mathbf{X}_T to escape suboptimal local minima.

Based on the unified upper bounds provided by Theorems 3 and 4, we propose incorporating $\mathcal{O}((\int \eta'(s)^2 ds)^\alpha)$ into Opt-Laws as a metric for evaluating the quality of the empirical loss values. In fact, the capacity to escape suboptimal local minima serves as an indicator of generalization capability. From this perspective, Opt-Laws not only includes convergence bounds from Theorems 3 and 4 to quantify optimization errors but also incorporates escape capacity to evaluate generalization errors. These two aspects together provide a comprehensive description of the final loss of LLMs.

6 Experiments

This section evaluates the usability, effectiveness, and accuracy of Opt-Laws framework across pre-training, continual training, and fine-tuning scenarios.

In all experiments, we utilized an $8 \times 0.6\text{B}$ MoE model (Zhao et al., 2024; Wei et al., 2024) with approximately 4B trainable parameters. Additionally, $8 \times 0.1\text{B}$ and $8 \times 0.3\text{B}$ MoE models, containing 0.5B and 2B learnable parameters, respectively, were employed in the pre-training experiments. All experiments were conducted with consistent token lengths and a batch size of 2048, using pre-training data sourced from the RedPajama-v2 dataset (Computer, 2023). For continual training, over 100B tokens from Chinese Common Crawl data were incorporated, while fine-tuning involved sampling an additional 60B+ tokens from the Stack-Repo Java code dataset (Shrivastava et al., 2023). *Detailed model parameters, along with the coefficients and exponents used in the opt-laws throughout the experiments, are thoroughly documented in Appendix Sec. A.*

The experiments are structured into four parts. First, we qualitatively assessed the impact of different LR schedules on pre-training loss, validating several conclusions derived from Opt-Laws. We then quantitatively evaluated Opt-Laws’ predictive capabilities by estimating the final pre-training loss. Subsequently, during continual training and fine-tuning, Opt-Laws, fitted with only small-scale pre-training loss data, were employed to rank various LR schedules. This ranking allowed us to identify the optimal candidate schedule prior to training, demonstrating the generalization capability of Opt-Laws. Although the predicted loss values were not directly meaningful for the unseen continual training and fine-tuning data, the relative ranking provided valuable guidance in selecting the most effective LR schedule.

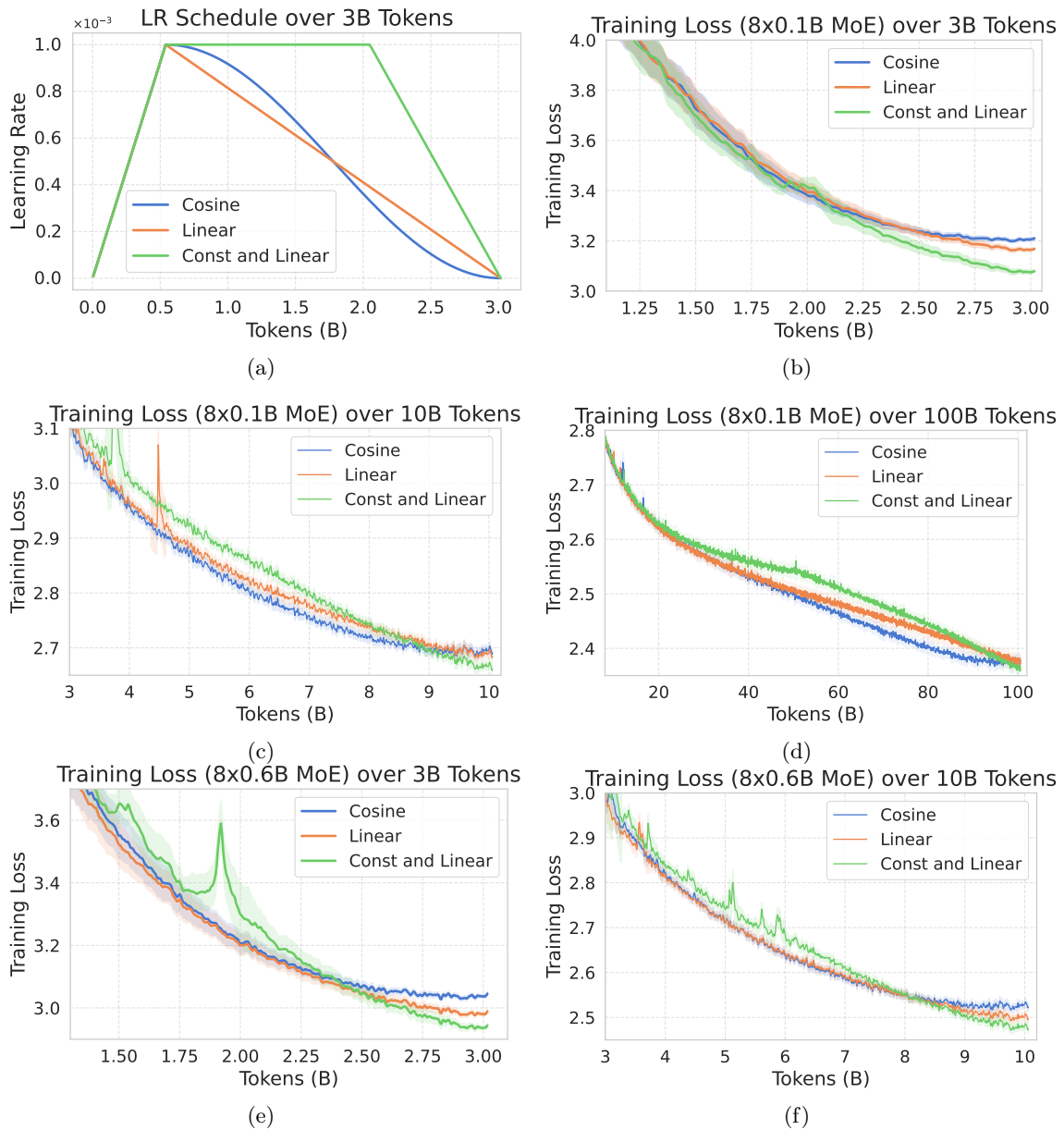


Figure 6: Training loss comparison for $8 \times 0.1B$ and $8 \times 0.6B$ MoEs under three LR schedules (linear decay, cosine decay, and constant followed by linear decay) across pre-training scales of 3B, 10B, and 100B tokens. Initial disparities in training loss at 3B tokens diminish with increased data volume, but larger model sizes slow the convergence of these gaps, highlighting the interplay between model scale and data volume as formulated by Opt-Laws.

6.1 Effects of Learning Rate Schedules

In this experiment, we systematically compared three distinct LR schedules across data scales of 3B, 10B, and 100B tokens. Each schedule began with a linear warmup phase,

gradually increasing from zero to a peak LR, η_{\max} . The cooldown strategies varied: one employed linear decay, another used cosine decay, and the third combined a constant rate with linear decay. The specific mathematical formulations of these LR schedules are provided in Eqn. (2) and Eqn. (3).

As depicted in Fig. 6, the results reveal notable differences in training loss across the LR schedules, particularly at the 3B token level. The LR schedule featuring a constant rate followed by linear decay ($\eta_{\text{const}}(\cdot)$) demonstrated superior performance in terms of final training loss compared to the other schedules. However, as the volume of training data increased, especially at the 100B token scale, the differences in training loss between the various schedules became negligible. This observation aligns with the insights discussed in Sec. 3.3.2, where it is suggested that the sensitivity of pre-training loss to LR schedules diminishes as data volume grows.

Although the diminishing influence of LR schedules on final training loss with increasing data volume may imply reduced importance, LR schedules remain critical, especially in the context of larger model size. As demonstrated in Fig. 6 (b) and (e), and further corroborated by Fig. 6 (c) and (f), the rate at which training losses converge under different LR schedules, slows markedly as model scale increases. For example, in Fig. 6 (c), training losses for the cosine decay and linear decay schedules nearly converge. However, in Fig. 6 (f), involving a model with 8 times more parameters, these schedules still exhibit considerable differences in training loss, despite identical token counts. This underscores the continued influence of LR schedules on training dynamics, particularly in scenarios with large models or moderate data volumes.

Additionally, as shown in Fig. 6 (b) and (c) at the 3B and 10B token levels, the linear decay schedule achieves a marginally lower final training loss compared to the cosine decay schedule ($\eta_{\text{cos}}(\cdot)$). This finding is particularly noteworthy because, despite the linear and cosine decay schedules being equivalent in terms of convergence components in Opt-Laws, they differ subtly in their ability to escape local minima. This capability is quantified by the integral $\int \eta_t'^2$, where the linear decay schedule exhibits a smaller integral value, correlating with its greater efficacy in achieving a lower final loss.

The empirical evidence presented in Fig. 6 aligns with the theoretical predictions of Opt-Laws, indicating that while the impact of LR schedules on final training loss diminishes with larger data volumes, their significance persists, particularly with increasing model size. These findings highlight the practical relevance of Opt-Laws in LLM training strategies, effectively linking theoretical results with empirical observations.

6.2 Opt-Laws for Pre-training

In this experiment, we employ generalized Opt-Laws, to predict the pre-training loss of large-scale models on extensive datasets. Specifically, we consider two MoE models: an $8 \times 0.6\text{B}$ model and an $8 \times 0.3\text{B}$ model. These models were pre-trained on 300B and 100B tokens of the English language dataset, respectively. We experiment with various hyper-parameter configurations, particularly different LRs η_1, η_2 and schedule parameters a_1, a_2 , and a_3 , as depicted in Fig. 4. The results, as shown in Table 1, compare the actual pre-training loss with the predictions generated by generalized Opt-Laws. Remarkably, Opt-Laws was able to predict the pre-training loss with a relative error of less than 0.1% across all configurations.

Table 1: Comparison of actual pre-training loss and predictions by Opt-Laws for various model sizes and LR schedules on 300B and 100B token datasets. The results demonstrate that Opt-Laws consistently predicts the pre-training loss with high accuracy across different configurations, with a relative error below 0.1%. The visualisation of η_1 , η_2 , a_1 , a_2 , and a_3 can be found in Fig. 4

| Model Size | Token Size | η_1 | η_2 | a_1 | a_2 | a_3 | Training Loss | Predicted Loss | Relative Error(%) |
|------------|------------|----------|----------|-------|-------|-------|---------------|----------------|-------------------|
| 8x0.6B | 300B | 1e-3 | 1e-3 | 500 | 500 | 500 | 1.985 | 1.984 | 0.04 |
| 8x0.6B | 300B | 6e-3 | 6e-3 | 2000 | 2000 | 2000 | 1.996 | 1.995 | 0.05 |
| 8x0.3B | 300B | 6e-3 | 6e-3 | 500 | 500 | 500 | 2.073 | 2.073 | 0.00 |
| 8x0.6B | 100B | 6e-4 | 6e-4 | 1200 | 1200 | 10000 | 2.076 | 2.075 | 0.04 |
| 8x0.6B | 100B | 1.2e-3 | 6e-4 | 1200 | 7000 | 13000 | 2.098 | 2.097 | 0.05 |
| 8x0.6B | 100B | 1.2e-3 | 6e-4 | 1200 | 5000 | 11500 | 2.097 | 2.096 | 0.04 |
| 8x0.6B | 100B | 1e-3 | 5e-4 | 5000 | 10000 | 15000 | 2.057 | 2.058 | 0.05 |
| 8x0.6B | 100B | 1e-3 | 1e-3 | 2000 | 2000 | 2000 | 2.077 | 2.078 | 0.05 |
| 8x0.6B | 100B | 1e-3 | 5e-4 | 2450 | 7000 | 12000 | 2.079 | 2.078 | 0.05 |
| 8x0.6B | 100B | 5e-5 | 5e-4 | 1000 | 1000 | 9500 | 2.077 | 2.078 | 0.05 |

The first three rows of Table 1 demonstrate that generalized Opt-Laws reliably predicts the pre-training loss for the 300B-token dataset, regardless of variations in model size or LR, capturing the loss with consistent accuracy across different configurations. Furthermore, when pre-training the 8×0.6 B model on 100B tokens, different selections of η_1 , η_2 , a_1 , a_2 , and a_3 generate complex learning rate schedules, resulting in significant variations in the final pre-training loss. Despite the complexity of these schedules, generalized Opt-Laws accurately predicted the final loss.

It is noteworthy that generalized Opt-Laws were fitted solely on loss data from small-scale models with simple learning rate schedules (linear warmup and linear cooldown) from Fig. 4. These fitted parameters and exponents, detailed in Appendix Sec. A, were then applied to the large-scale scenarios here. Nevertheless, generalized Opt-Laws exhibited a strong capacity to generalize to more complex LR schedules during the evaluations.

To further substantiate the reliability of generalized Opt-Laws, we utilized it to infer specific combinations of η_1 , η_2 , a_1 , a_2 , and a_3 (as shown in the last three rows of Table 1) that would yield same predicted losses. We then pre-trained the 8×0.6 B MoEs on 100B tokens using these inferred LR schedules. Fig. 7 presents these schedules alongside their corresponding training loss curves. The training losses converged to nearly the same value across all three schedules, confirming the effectiveness and accuracy of generalized Opt-Laws in predicting the final training loss, even under varying and complex LR strategies.

The findings from these experiments imply that, in practical scenarios, we can leverage small-scale models and datasets to extrapolate the final loss for large-scale models using generalized Opt-Laws. This approach significantly reduces the computational cost and time required for training LLMs. Additionally, generalized Opt-Laws offers the capability to filter out hyper-parameter combinations that might lead to training instability and identify those likely to be optimal, thereby reducing the need for extensive hyper-parameter tuning.

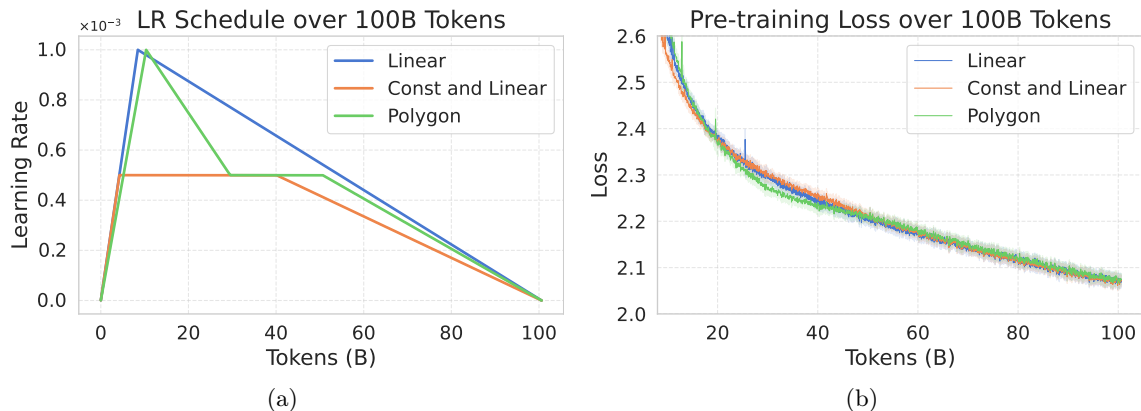


Figure 7: Training loss curves for three distinct LR schedules applied to the 8x0.6B model on the 100B token dataset. Despite substantial differences in the schedules, the losses converge to nearly the same final value, in line with Opt-Laws’s predictions, demonstrating its effectiveness in accurately forecasting training outcomes.

6.3 Opt-Laws for Continual Training

This experiment explores the application of generalized Opt-Laws to evaluate the effectiveness of different LR schedules during the continual training of LLMs. Continual training, unlike pre-training, involves further training an already partially trained model on new datasets, which are typically comparable in size to the original pre-training data. Given that the LR has often decayed to a low value by the end of pre-training, it becomes necessary in continual training to first increase the LR and then reduce it gradually to ensure optimal performance on the new data. The challenge of appropriately adjusting the LR and selecting the most effective LR schedule is crucial, as it can significantly impact model performance on the new data. This experiment investigates how Opt-Laws can assist in pre-selecting an optimal LR schedule, thereby reducing the computational cost associated with hyper-parameter tuning.

In this experiment, we utilized an $8 \times 0.6\text{B}$ MoE model, pre-trained on 300B tokens of English data from the RedPajama-v2 dataset. The LR schedule used during pre-training is detailed in Table 1, row one. We evaluate two scenarios: (1) a scenario with weak distribution shift between the pre-training and continual training data, and (2) a scenario with a strong data distribution shift.

In the weak distribution shift scenario, we sampled another 100B tokens from the RedPajama-v2 dataset for continual training and tested five distinct LR schedules. The results are illustrated in Fig. 8. Fig. 8 (a) displays the LR schedules, while Fig. 8 (b) shows the corresponding loss curves throughout the training process. Although the LR schedules differed significantly, and this was reflected in the loss curves, the final loss values were relatively close across all schedules. This suggests that when the peak LR is appropriately set, and the data distribution shift is weak, the choice of LR schedule has a limited impact on the final model performance. This finding is consistent with previous observations in small-scale models (Ibrahim et al., 2024), and we extend this validation to a larger scale.

In the scenario of a strong distribution shift, we used approximately 100B tokens of Chinese common crawl data for continual training. Due to the significant divergence between

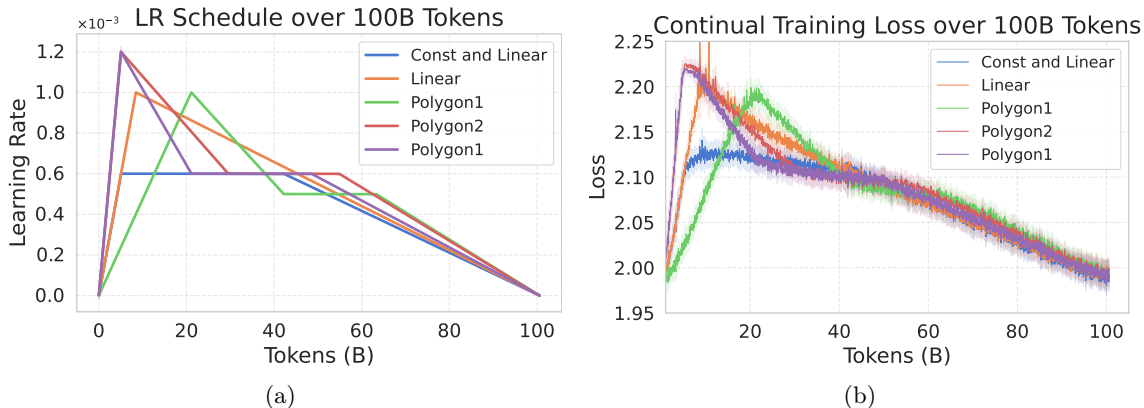


Figure 8: Loss curves for continual training under five different learning rate schedules with weak data distribution shift. (a) shows the LR schedules, while (b) depicts the resulting loss trajectories. Despite the variance in LR schedules, final losses converge closely, suggesting a limited impact of the LR schedule on final performance when the data distribution shift is weak.

Table 2: Predicted vs. actual final loss rankings for different LR schedules during continual training under a strong data distribution shift. The LR schedule hyper-parameters η_1, η_2 , and $a_1 - a_3$ were pre-selected using generalized Opt-Laws prior to training, ensuring both a clear predicted loss ranking and sufficient gaps between losses to maintain distinctiveness. generalized Opt-Laws accurately predicts the relative order of final losses, validating its utility in selecting optimal LR schedules.

| Setting | Model Size | Token Size | η_1 | η_2 | a_1 | a_2 | a_3 | Actual Loss | Actual Ranking | Predicted Ranking |
|---------|------------|------------|----------|----------|-------|-------|-------|-------------|----------------|-------------------|
| ① | 8x0.6B | 100B | 1e-3 | 5e-4 | 5000 | 10000 | 15000 | 1.826 | ①>②>③ | ①>②>③ |
| ② | 8x0.6B | 100B | 1.2e-3 | 6e-4 | 1200 | 7000 | 13000 | 1.821 | | |
| ③ | 8x0.3B | 100B | 1e-3 | 1e-3 | 2000 | 2000 | 2000 | 1.818 | | |

the continual training and pre-training datasets, we employed a replay mechanism, informed by prior research (Parmar et al., 2024; Guo et al., 2024; Ke et al., 2023). Specifically, we mixed 5% of the original pre-training English data with the continual training data, resulting in a final dataset of 95B Chinese tokens and 5B English tokens.

Given that the Opt-Laws parameters were initially calibrated using loss values from the pre-training phase, excluding sample loss points from continual training on Chinese data, Opt-Laws could only predict the relative ranking of final losses across different LR schedules during continual training, rather than their absolute values. To effectively apply Opt-Laws in continual training, we needed to modify the original **Opt-Laws**.

Experimental observations suggest that model convergence during continual training occurs more rapidly under the same LR schedules compared to pre-training. This prompted an adjustment of the escape term in the Opt-Laws formula, hypothesizing that continual

Table 3: Performance comparison of different LR schedules during fine-tuning across varying dataset sizes (3B, 30B, 60B tokens). The table shows that Opt-Laws successfully identify the optimal LR schedule candidate and accurately rank the final fine-tuning loss, demonstrating its effectiveness in hyper-parameter selection.

| Setting | Model Size | Token Size | η_1 | η_2 | a_1 | a_2 | a_3 | Actual Loss | Actual Ranking | Predicted Ranking |
|---------|------------|------------|----------|----------|-------|-------|-------|-------------|----------------|-------------------|
| ① | 8x0.6B | 3B | 5e-4 | 5e-4 | 128 | 128 | 128 | 0.920 | ①>②>③ | ①>②>③ |
| ② | 8x0.6B | 3B | 1e-3 | 1e-3 | 512 | 512 | 512 | 0.909 | | |
| ③ | 8x0.3B | 3B | 1.5e-3 | 1.5e-3 | 128 | 128 | 128 | 0.904 | | |
| ① | 8x0.6B | 30B | 5e-4 | 5e-4 | 128 | 128 | 128 | 0.857 | ①>②>③ | ①>②>③ |
| ② | 8x0.6B | 30B | 1e-3 | 1e-3 | 512 | 512 | 512 | 0.849 | | |
| ③ | 8x0.3B | 30B | 1.5e-3 | 1.5e-3 | 128 | 128 | 128 | 0.847 | | |
| ① | 8x0.6B | 60B | 5e-4 | 5e-4 | 128 | 128 | 128 | 0.822 | ②>①>③ | ②>①>③ |
| ② | 8x0.6B | 60B | 2e-3 | 2e-3 | 512 | 512 | 512 | 0.817 | | |
| ③ | 8x0.3B | 60B | 3e-4 | 3e-4 | 128 | 128 | 7000 | 0.826 | | |

training dynamics allow for faster escape from local minima. Specifically, inspired by Theorem 3 and Theorem 4, we replaced the term $\int_{a_{e_2}}^S \eta_t'^2$ with $\int_{a_{e_2}}^S \eta_t'^2 / \eta_{\max}^4$, where η_{\max} denotes the maximum LR during the interval $[a_{e_2}, S]$. This modification increases the influence of the escape term without requiring further adjustments to the coefficient vector \mathbf{c} or the exponent vector $\boldsymbol{\alpha}$. When selecting the vectors \mathbf{a}_c and \mathbf{a}_e for the continual training LR schedule η_t^{ft} , it is crucial to follow the method outlined in Sec. 4.3, while also accounting for the pre-training LR schedule η_t^{pre} . Neglecting the pre-training LR schedule would obscure the distinction between continual training and pre-training. Specifically, the integral term $\int_0^{a_{c_1}} \eta_t$ must incorporate contributions from both the pre-training and continual training schedules. Therefore, we let $\int_0^{a_{c_1}} \eta_t = \int_0^{S^{pre}} \eta_t^{pre} + \int_0^{a_{c_1}} \eta_t^{ft}$, where S^{pre} represents the number of iterations during pre-training, and a_{c_1} is selected based on the schedule η_t^{ft} . No further modifications to other components are required.

The modified Opt-Laws formula successfully predicts the relative ranking of final losses for different LR schedules in continual training, as shown in Table 2. Interestingly, this ranking differs from that observed during pre-training with the same LR schedules, highlighting the effectiveness and robustness of Opt-Laws. It is crucial to note that these formula adjustments are not simply a forced fit to our numerical results. The revised formula also demonstrates its effectiveness in predicting relative rankings in fine-tuning experiments (as detailed in Sec. 6.4), further validating Opt-Laws as a practical and reliable tool for selecting optimal LR schedule candidates.

6.4 Opt-Laws for Fine-Tuning

In this section, we investigate the use of generalized Opt-Laws to predict fine-tuning loss on large-scale models when applied to specialized datasets. Fine-tuning, distinct from

pre-training and continual training, typically involves refining model parameters using a small-scale, higher-quality dataset from a specific domain with the goal of enhancing the model’s performance in a targeted area.

In our experiments, we fine-tuned an $8 \times 0.6\text{B}$ MoE model on the Stack-Repo Java code dataset. Prior to fine-tuning, the model had been pre-trained on 300B tokens of English text and subsequently underwent continual training on 100B tokens of Chinese language data. We conducted fine-tuning with three different token counts, 3B, 30B, and 60B, across three different LR schedules, as detailed in Table 3.

To evaluate the effectiveness of generalized Opt-Laws in this context, we applied the same methodology used in the continual training experiment to modify generalized Opt-Laws. Subsequently, we utilized generalized Opt-Laws to rank the different LR schedules corresponding to each dataset size, aiming to identify the LR schedule that would minimize loss prior to actual training.

In both the 3B and 30B token scenarios, generalized Opt-Laws’s loss predictions indicated that the difference between settings ① and ② was significantly greater than that between settings ② and ③. This suggests that the loss for setting ① is likely to be significantly higher than for the other two settings, which is consistent with the actual losses observed in Table 3. Additionally, as the training data size increases from 3B to 30B tokens, the difference between the loss values predicted by generalized Opt-Laws for settings ② and ③ narrows rapidly, a trend that closely aligns with the empirical results shown in Table 3. These results demonstrate that generalized Opt-Laws not only successfully identified the optimal LR schedule for each dataset size but also accurately predicted the final ranking of the three LR schedules, validating its accuracy and effectiveness in hyper-parameter selection for fine-tuning.

This experiment extends the applicability of generalized Opt-Laws, illustrating its utility in selecting fine-tuning hyper-parameters without requiring additional data or parameter re-calibration. The results in Table 3 further validate the generalization capabilities and effectiveness of generalized Opt-Laws, highlighting its significant potential in hyper-parameter selection for fine-tuning.

7 Conclusion

In this work, we introduced Opt-Laws, a novel method for hyper-parameters selection in large-scale LLM training. By leveraging data from smaller-scale models, Opt-Laws establishes mathematical relationships between training hyper-parameters and final training loss, enabling the pre-selection of optimal configurations before full-scale training. Our approach uniquely employs SDEs to analyze first-order optimization algorithms, focusing on convergence rates and escape probabilities from local minima. Notably, we are the first to employ SDEs to establish the convergence rate of gradient methods for non-convex optimization problems and to apply time-inhomogeneous SDEs for evaluating escape probabilities in non-convex settings. Through extensive experiments on models with over 4B parameters and various datasets, we demonstrated Opt-Laws’s effectiveness across pre-training, continual training, and fine-tuning scenarios, highlighting its potential to significantly reduce the computational cost and complexity of hyper-parameter tuning in large-scale LLMs training.

Appendix A. Additional Experimental Results

This section provides supplementary information not covered in the main text, including details on model architecture, parameters, and standardized training settings. Additionally, we present the fitted coefficients $*c$ of the opt-laws, the Power α , and the analytical expressions for the 16-dimensional optimization-feature vector under two specific LR schedules.

A.1 Model Parameters and Structure

Table 4 summarizes the key parameters of the MoE model employed in our experiments. These include architectural parameters such as the number of layers, hidden size, and the number of attention heads, along with parameter sizes: total trainable parameters, activated parameters during the forward pass, and the total parameters for the eight experts. Additionally, common training parameters are listed, including token length, global batch size, optimizer (AdamW (Loshchilov and Hutter, 2017)), weight decay, minimal learning rate, and gradient clipping threshold. These parameters adhere to standard LLM training practices without any special adjustments. We set the minimal learning rate to 0.0 for two reasons. First, while some approaches use a minimal LR of $0.1\eta_{\max}$, this can hinder comparability between different LR schedules, as a higher minimal LR often results in suboptimal final training loss. Second, setting the minimal LR to 0.0 can enhance model performance, which is our primary objective. Therefore, to maximize the model’s potential, we opted for a minimal learning rate of 0.0.

Table 4: Overview of key parameters for the MoE models, detailing architectural configurations (e.g., layers, hidden size, attention heads) and shared training settings (e.g., token length, batch size, optimizer).

| Model Size | Layer Num. | Hidden Size | Num. of AttnHead | Total Param. | Activated Param. | Expert Param. | Token Length | Batch Size | Opt. | Weight Decay | Min. LR | Grad. Clip |
|--------------------------|------------|-------------|------------------|--------------|------------------|---------------|--------------|------------|-------|--------------|---------|------------|
| $8 \times 0.001\text{B}$ | 4 | 128 | 4 | 0.023B | 0.019B | 0.0063B | 2048 | 2048 | AdamW | 0.1 | 0.0 | 1.0 |
| $8 \times 0.02\text{B}$ | 12 | 384 | 12 | 0.17B | 0.093B | 0.113B | | | | | | |
| $8 \times 0.1\text{B}$ | 12 | 768 | 12 | 0.58B | 0.27B | 0.45B | | | | | | |
| $8 \times 0.3\text{B}$ | 24 | 1024 | 16 | 1.90B | 0.75B | 1.66B | | | | | | |
| $8 \times 0.6\text{B}$ | 24 | 1536 | 16 | 4.05B | 1.56B | 3.62B | | | | | | |

A.2 Coefficient for Opt-Laws

In Tables 5 and 6, we summarize the coefficients of the Opt-Laws used for large-scale hold-out and out-of-distribution experiments. By performing linear regression on the loss data in Fig. 2, we get the coefficient vector \mathbf{c} , which is presented alongside the manually set powers vector α in Tables 5 and 6. Unlike the Opt-Laws in Eqn. (1), the coefficient vector \mathbf{c} for generalized Opt-Laws is not constrained to be strictly positive. This flexibility arises because the sign of a coefficient does not necessarily indicate a straightforward positive or negative correlation with the target variable. For example, the training loss is positively correlated

Table 5: This table provides the coefficients, fitted using Fig. 2, and the manually set powers for the convergence and escape terms in **Opt-Laws**. It also includes the analytical expressions for these terms under two distinct LR schedules: (1) a linear warmup over a steps followed by a linear cooldown over $S - a$ steps, and (2) a linear warmup over a_1 steps, a constant LR ($h = \eta_{\max}$) from a_1 to a_2 steps, and a cooldown over $S - a_2$ steps.

| | Convergence Terms | | | | Escape Terms | | | |
|---|---------------------------|---------------------------|-------------------------------------|---|------------------------------|------------------------------|------------------------------|----------|
| | $\int_0^{a_{c_1}} \eta_t$ | $\int_{a_{c_2}}^S \eta_t$ | $\frac{N}{\int_{a_{c_2}}^S \eta_t}$ | $\int_0^{a_{c_1}} \eta_t \int_{a_{c_2}}^S \eta_t$ | $\int_{a_{e_2}}^S \eta_t'^2$ | $\int_0^{a_{e_1}} \eta_t'^2$ | $\int_{a_{e_2}}^S \eta_t'^2$ | SN |
| Power α | -1.0 | -1.0 | 0.25 | -0.23 | 1.0 | 0.25 | 0.25 | -0.25 |
| Coeff. \mathbf{c} | -6.92e-4 | -1.27e-3 | -4.68e-2 | 4.65e-2 | 9.62e-3 | 1.92e-2 | -5.05e-2 | -1.82e-1 |
| Linear Warm. & Cooldown $a_{c_i} = a_{e_i} = a$ | $\frac{1}{2}ah$ | $\frac{(S-a)h}{2}$ | $\frac{2N}{(S-a)h}$ | $\frac{a(S-a)h^2}{4}$ | $\frac{h^2}{S-a}$ | $\frac{h^2}{a}$ | $\frac{h^2}{S-a}$ | SN |
| Const. & Cooldown $a_{c_i} = a_{e_i} = a_1$ | $\frac{1}{2}a_1h$ | $\frac{(S+a_2-2a_1)h}{2}$ | $\frac{2N}{(S+a_2-2a_1)h}$ | $\frac{a(S+a_2-2a_1)h^2}{4}$ | $\frac{h^2}{S-a_2}$ | $\frac{h^2}{a_1}$ | $\frac{h^2}{S-a_2}$ | SN |

with both $\int_{a_{e_2}}^S \eta_t'^2$ and $1/\int_0^{a_{c_1}} \eta_t$. It is then also positively correlated with the expression $(\int_{a_{e_2}}^S \eta_t'^2 - b)/\int_0^{a_{c_1}} \eta_t$, where $b > 0$ is a constant with a proper range. This illustrates that when quadratic terms, such as products of variables, are introduced, a negative coefficient on $1/\int_0^{a_{c_1}} \eta_t$ does not imply a negative correlation with training loss. Therefore, we do not impose positivity constraints on the coefficient vector \mathbf{c} in the linear regression.

Before estimating the model loss using the parameters from these tables, it is necessary to normalize the training iteration steps S , model size N , and LR. For model parameter count N , we use the total number of learnable parameters, expressed in billions. Similarly, S and all other iteration-related variables (e.g., warmup steps, cooldown steps) are converted to a token-based metric (in billions) by computing steps \times token size \times global batch size $/10^9$. The LR is normalized by dividing it by 1.5×10^{-2} , ensuring that the normalized LR values fall within the range of 0 to 1 across all experiments.

Table 5 provides the coefficients and powers for the convergence and escape terms, while Table 6 lists those for the mixed and bias terms. Both tables consider two specific LR schedules: (1) a linear warmup over a steps followed by a linear cooldown over $S - a$ steps, and (2) a linear warmup over a_1 steps, followed by a constant LR (η_{\max}) from a_1 to a_2 steps, and a cooldown over $S - a_2$ steps (as illustrated in Fig. 6 (a)). For these two LR schedules, we present the corresponding analytical expressions for the optimization-feature vector, facilitating further validation of the **Opt-Laws** under real large-scale training cases.

A.3 Coefficient for Criterion

We now present the coefficients and power terms in the criterion $R(\eta_{\max}, a_1, N, S)$ as defined in Eqn. 4. Before using $R(\eta_{\max}, a_1, N, S)$ to determine whether the training hyper-parameters

Table 6: This table presents the coefficients, derived from Fig. 2, and the manually set powers for the mixed and bias terms in **Opt-Laws**. It also includes the analytical expressions for these terms corresponding to the same two LR schedules: (1) a linear warmup over a steps followed by a linear cooldown over $S - a$ steps, and (2) a linear warmup over a_1 steps, a constant LR ($h = \eta_{\max}$) from a_1 to a_2 steps, and a cooldown over $S - a_2$ steps.

| | Mixed Terms | | | | Bias Terms | | | |
|---|--|--|--|--|------------|---------|---------------|---------|
| | $\frac{\int_{a_{e_2}}^S \eta_t'^2}{\int_0^{a_{c_1}} \eta_t}$ | $\frac{\int_{a_{e_2}}^S \eta_t'^2}{\int_{a_{c_2}}^S \eta_t}$ | $\frac{N \int_{a_{e_2}}^S \eta_t'^2}{\int_0^{a_{c_1}} \eta_t}$ | $\frac{N \int_{a_{e_2}}^S \eta_t'^2}{\int_{a_{c_2}}^S \eta_t}$ | N | S | η_{\max} | 1.0 |
| Power α | 0.2 | 0.15 | 0.15 | 0.15 | -0.25 | -0.25 | 0.2 | 1.0 |
| Coeff. \mathbf{c} | -4.68e-2 | -4.18e-2 | -1.19e-1 | 2.18e-1 | 3.1e-1 | 6.98e-1 | 5.26e-2 | 3.14e-1 |
| Linear Warm. & Cooldown $a_{c_i} = a_{e_i} = a$ | $\frac{2h}{a(S-a)}$ | $\frac{2h}{(S-a)^2}$ | $\frac{2hN}{a(S-a)}$ | $\frac{2hN}{(S-a)^2}$ | N | S | h | 1.0 |
| Const. & Cooldown $a_{c_i} = a_{e_i} = a_1$ | $\frac{2h}{a_1(S-a_2)}$ | $\frac{2h}{(S-a_2)(S+a_2-2a_1)}$ | $\frac{2hN}{a_1(S-a_2)}$ | $\frac{2hN}{(S-a_2)(S+a_2-2a_1)}$ | N | S | h | 1.0 |

will cause divergence, it is crucial to normalize the training iteration step S , warmup step a_1 , model size N , and peak LR η_{\max} following the same approach outlined previously in Sec. A.2. Additionally, after normalization, we apply further pre-processing to the normalized values \hat{S} and \hat{a}_1 by setting $S = \hat{S}^2$ and $a_1 = \hat{a}_1^2$. These adjusted values of S and a_1 are then substituted into $R(\eta_{\max}, a_1, N, S)$ to evaluate whether the current hyper-parameter configuration may lead to divergence. The data-driven parameters in $R(\eta_{\max}, a_1, N, S)$, obtained by fitting the loss data from Fig. 2, are $\hat{c}_1 = 1.76$, $\hat{c}_2 = 33.21$, $\hat{c}_3 = 292.03$, $\hat{\alpha}_1 = 0.218$, and $\hat{\alpha}_2 = 0.5$.

Appendix B. Analysis for Opt-Laws, SGD-SDE, and Adam-SDE

B.1 Proof of Proposition 1

Proof Based on the proposed Opt-Laws, the analytical expressions for the two LR schedules, $\eta_{\cos}(t)$ and $\eta_{\text{const}}(t)$, can be derived as follows:

$$\begin{aligned}
 \text{Opt-Laws}(\eta_{\cos}) &= c_1 \left(\frac{2}{\eta_{\max} a} \right)^{\alpha_1} + c_2 \left(\frac{2}{\eta_{\max} (S-a)} \right)^{\alpha_2} + \frac{c_3}{S} + b \\
 &\quad + c_4 \left(\frac{\pi^2 \eta_{\max}^2}{8(S-a)} \right)^{\alpha_3} + c_5 \left(\frac{\eta_{\max}^2}{a} \right)^{\alpha_4}. \\
 \text{Opt-Laws}(\eta_{\text{const}}) &= c_1 \left(\frac{2}{\eta_{\max} a} \right)^{\alpha_1} + c_2 \left(\eta_{\max} (a_c - a) + \frac{\eta_{\max} (S - a_c)}{2} \right)^{-\alpha_2} \\
 &\quad + \frac{c_3}{S} + b + c_3 \left(\frac{\eta_{\max}^2}{S - a_c} \right)^{\alpha_3} + c_5 \left(\frac{\eta_{\max}^2}{a} \right)^{\alpha_4}.
 \end{aligned}$$

Note that $\lim_{S \rightarrow \infty} \text{Opt-Laws}(\eta_{\cos}(\cdot)) = \lim_{S \rightarrow \infty} \text{Opt-Laws}(\eta_{\text{const}}(\cdot)) = b$. Therefore, we have $\lim_{S \rightarrow \infty} |\text{Opt-Laws}(\eta_{\cos}(\cdot)) - \text{Opt-Laws}(\eta_{\text{const}}(\cdot))| = 0$. \blacksquare

B.2 Derivations for SGD-SDE and Adam-SDE

In this subsection, we derive the SDEs to model the iterative SGD and Adam sequences.

SGD-SDE: The iterative sequence of SGD is given by

$$\mathbf{x}_{k+1} = \mathbf{x}_k - \eta_0 \eta_k (\nabla f(\mathbf{x}_k) + \mathbf{z}_k), \quad \mathbf{z}_k \sim \mathcal{N}(0, \Sigma(\mathbf{x}_k)), \quad (22)$$

where η_k is the normalized learning rate, η_0 is a small rescaling parameter, and ξ_k is a Gaussian noise. Applying the Euler-Maruyama method (for a detailed description, see (Särkkä and Solin, 2019, Chapter 8.2)) to the corresponding SDE (SGD-SDE), we obtain:

$$\mathbf{x}_{k+1} = \mathbf{x}_k - \eta(t_k) \nabla f(\mathbf{x}_k) \Delta t_{k+1} + \sqrt{\eta_0} \eta(t_k) (\Delta t_{k+1} \Sigma(\mathbf{x}_k))^{\frac{1}{2}} \Delta \mathbf{W}_k,$$

where $\Delta t_{k+1} = t_{k+1} - t_k$ and $\Delta \mathbf{W}_k \sim \mathcal{N}(0, \mathbf{I}_N)$. By setting $\Delta t_{k+1} \equiv \eta_0$, the discrete scheme exactly recovers the SGD sequence (22). With the same initial conditions, where $\mathbf{x}_0 = \mathbf{X}_0$, and under certain smooth regularity conditions on the functions involved, it can be established that a positive constant $\alpha > 0$ (referred to as the order) exists satisfying the following property. For any time horizon $T > 0$ and positive integer $m \leq \lfloor \frac{T}{\eta_0} \rfloor$, there exists a constant K and a sufficiently small η_0 such that the following strong error bound holds

$$\mathbb{E} [\|\mathbf{X}_{m\eta_0} - \mathbf{x}_m\|] \leq K \eta_0^\alpha.$$

The classical approximation order for the Euler-Maruyama method is typically $\alpha = \frac{1}{2}$, which was proven in Gihman and Skorohod (1979). We do not delve into the details on this topic, as it is beyond the scope of this work. For a comprehensive discussion on the error analysis of numerical approximations for SDEs, interested readers may consult Kloeden and Platen (1999); Särkkä and Solin (2019). Additionally, for insights into the errors associated with modeling SGD sequences using SDEs, one can refer to the works of Li et al. (2019, 2021).

Adam-SDE: By applying the Euler-Maruyama method for the SDE associated with \mathbf{m}_t in (Adam-SDE), we obtain:

$$\begin{aligned} \mathbf{m}_{k+1} &= \mathbf{m}_k - c_1 \eta(t_k) (\mathbf{m}_k - \nabla f(\mathbf{x}_k)) \Delta t_{k+1} + c'_1 \eta(t_{k+1}) (\Delta t_{k+1} \Sigma(\mathbf{x}_k))^{\frac{1}{2}} \Delta \mathbf{W}_k \\ &= (1 - c_1 \Delta t_{k+1} \eta_k) \mathbf{m}_k + c_1 \Delta t_{k+1} \eta_k \left(\nabla f(\mathbf{x}_k) + \frac{c'_1}{c_1 \sqrt{\Delta t_{k+1}}} (\Sigma(\mathbf{x}_k))^{\frac{1}{2}} \Delta \mathbf{W}_k \right). \end{aligned}$$

Setting $\Delta t_{k+1} = \frac{\hat{c}_1}{c_1}$ and $c'_1 = c_1 \sqrt{\Delta t_{k+1}} = \sqrt{c_1 \hat{c}_1}$, we derive that

$$\mathbf{m}_{k+1} = (1 - \beta_{1,k}) \mathbf{m}_k + \beta_{1,k} (\nabla f(\mathbf{x}_k) + \mathbf{z}_k),$$

where $\beta_{1,k} = 1 - \hat{c}_1 \eta_k$, $\mathbf{z}_k \sim \mathcal{N}(0, \Sigma(\mathbf{x}_k))$. This recovers the update of $\{\mathbf{m}_k\}$ in (Adam). Furthermore, the update of \mathbf{x}_k corresponds to Euler's method for the ODE associated with \mathbf{X}_t in (Adam-SDE). The update of \mathbf{v}_k aligns with the SDE associated with \mathbf{v}_t in (Adam-SDE), which directly follows from (Malladi et al., 2022, Theorem 4.2 or Theorem 4.5).

B.3 Proof of Proposition 2

Proof Let $\mathbf{z}_i := \nabla F(\mathbf{x}, \zeta_i) - \nabla f(\mathbf{x})$ and $\mathbf{Z} := [\mathbf{z}_1, \mathbf{z}_2, \dots, \mathbf{z}_D]$, then $\boldsymbol{\Sigma}(\mathbf{x}) = \frac{1}{D} \mathbf{Z} \mathbf{Z}^\top$. Therefore, $\text{Tr}(\boldsymbol{\Sigma}(\mathbf{x})) = \frac{1}{D} \sum_{i=1}^D \text{Tr}(\mathbf{z}_i \mathbf{z}_i^\top) = \frac{1}{D} \sum_{i=1}^D \|\mathbf{z}_i\|^2$. Note that $\mathbf{z}_i \sim N(0, \boldsymbol{\Sigma}_g)$ are i.i.d. Gaussian vectors, where $\boldsymbol{\Sigma}_g$ is an $N \times N$ positive semidefinite covariance matrix. So next, we analyze the concentration of $\frac{1}{D} \sum_{i=1}^D \|\mathbf{z}_i\|^2$. Each $\|\mathbf{z}_i\|^2$ can be represented as a sum of weighted χ^2 variables:

$$\|\mathbf{z}_i\|^2 \sim \sum_{j=1}^n \lambda_j \chi_{ij}^2,$$

where λ_j are the eigenvalues of $\boldsymbol{\Sigma}_g$. The expected value and variance of $\|\mathbf{z}_i\|^2$ are given by:

$$\mathbb{E}[\|\mathbf{z}_i\|^2] = \text{tr}(\boldsymbol{\Sigma}_g), \quad \text{Cov}(\|\mathbf{z}_i\|^2) = 2 \text{Tr}(\boldsymbol{\Sigma}_g^2).$$

Given that χ^2 distribution is sub-exponential, we apply Bernstein's inequality to estimate the concentration of $\frac{1}{D} \sum_{i=1}^D \|\mathbf{z}_i\|^2$, which is given by:

$$\mathbb{P} \left(\left| \frac{1}{D} \sum_{i=1}^D \|\mathbf{z}_i\|^2 - \text{Tr}(\boldsymbol{\Sigma}_g) \right| \geq t \right) \leq 2 \exp \left(- \frac{Dt^2}{4 \text{Tr}(\boldsymbol{\Sigma}_g^2) + 2t \|\boldsymbol{\Sigma}_g\|_{\text{op}}} \right),$$

where $\|\boldsymbol{\Sigma}_g\|_{\text{op}}$ is the operator norm (largest eigenvalue) of $\boldsymbol{\Sigma}_g$. This completes the proof. \blacksquare

B.4 Proof of Proposition 3

Proof Let $\mathbf{Z}_i := \boldsymbol{\Sigma}_g^{-\frac{1}{2}} (\nabla F(\mathbf{x}, \zeta_i) - \nabla f(\mathbf{x}))$ and $\mathbf{Z} := [\mathbf{Z}_1, \mathbf{Z}_2, \dots, \mathbf{Z}_D]$. Then, $\{\mathbf{Z}_i\}$ are standard Gaussian variables. Let $\hat{\boldsymbol{\Sigma}}(\mathbf{x}) := \frac{1}{D} \mathbf{Z} \mathbf{Z}^\top$. By the eigenvalue variance bounds for covariance matrices in (Ledoux and Rider, 2010, Corollary 3), there exists a constant $C > 0$ such that

$$\begin{aligned} \mathbb{E} \left[\lambda_{\max}(\hat{\boldsymbol{\Sigma}}(\mathbf{x})) \right] &\leq \mathbb{E} \left[\left| \lambda_{\max}(\hat{\boldsymbol{\Sigma}}(\mathbf{x})) - \left(1 + \sqrt{\frac{D}{N}} \right) \right| \right] + \left(1 + \sqrt{\frac{D}{N}} \right) \\ &\leq \sqrt{\mathbb{E} \left[\left(\lambda_{\max}(\hat{\boldsymbol{\Sigma}}(\mathbf{x})) - \left(1 + \sqrt{\frac{D}{N}} \right) \right)^2 \right]} + \left(1 + \sqrt{\frac{D}{N}} \right) \\ &\leq \frac{C}{N^{\frac{2}{3}}} + \left(1 + \sqrt{\frac{D}{N}} \right). \end{aligned}$$

Furthermore, note that $\boldsymbol{\Sigma}(\mathbf{x}) = \boldsymbol{\Sigma}_g^{\frac{1}{2}} \hat{\boldsymbol{\Sigma}}(\mathbf{x}) \boldsymbol{\Sigma}_g^{\frac{1}{2}}$, it follows that:

$$\mathbb{E} [\lambda_{\max}(\boldsymbol{\Sigma}(\mathbf{x}))] \leq \|\boldsymbol{\Sigma}_g\|_{\text{op}} \mathbb{E} \left[\left\| \hat{\boldsymbol{\Sigma}}(\mathbf{x}) \right\|_{\text{op}} \right] = \left(1 + \sqrt{\frac{D}{N}} \right) \sigma_g^2 + \frac{C \sigma_g^2}{N^{\frac{2}{3}}},$$

where $\|\cdot\|_{\text{op}}$ is the operator norm of matrix. This completes the proof. \blacksquare

Appendix C. Proofs for Convergence Analysis

C.1 Proof of Theorem 1

Proof Apply the Itô formula to $f(\mathbf{X}_t)$ and utilize the definition of (SGD-SDE), we obtain:

$$\begin{aligned} df(\mathbf{X}_t) &= \langle \nabla f(\mathbf{X}_t), d\mathbf{X}_t \rangle + \frac{1}{2} \langle \nabla^2 f(\mathbf{X}_t) d\mathbf{X}_t, d\mathbf{X}_t \rangle \\ &= -\eta(t) \|\nabla f(\mathbf{X}_t)\|^2 dt + \eta_0 \eta(t) \langle \nabla f(\mathbf{X}_t), \sigma(\mathbf{X}_t) d\mathbf{W}_t \rangle \\ &\quad + \frac{\eta_0 \eta(t)^2}{2} \langle \nabla^2 f(\mathbf{X}_t), \sigma(\mathbf{X}_t) \sigma(\mathbf{X}_t)^\top \rangle dt. \end{aligned}$$

Taking the integral and then taking the expectation, we have:

$$\begin{aligned} \mathbb{E}[f(\mathbf{X}_t) - f(\mathbf{X}_0)] &= -\mathbb{E} \left[\int_0^t \eta(s) \|\nabla f(\mathbf{X}_s)\|^2 ds \right] \\ &\quad + \mathbb{E} \left[\int_0^t \frac{\eta_0 \eta(s)^2}{2} \langle \nabla^2 f(\mathbf{X}_s), \sigma(\mathbf{X}_s) \sigma(\mathbf{X}_s)^\top \rangle ds \right] \\ &\leq -\mathbb{E} \left[\int_0^t \eta(s) \|\nabla f(\mathbf{X}_s)\|^2 ds \right] + \left(\frac{\eta_0 L N}{2} \int_0^t \eta(s)^2 ds \right) \sup_{\mathbf{x} \in \mathbb{R}^N} \mathbb{E}[\|\Sigma(\mathbf{x}_s)\|_{\text{op}}]. \end{aligned}$$

Rearranging the terms and dividing both sides by $\int_0^t \eta(s) ds$, and by Proposition 3, we have

$$\mathbb{E} \left[\frac{\int_0^t \eta(s) \|\nabla f(\mathbf{X}_s)\|^2 ds}{\int_0^t \eta(s) ds} \right] \leq \frac{f(\mathbf{X}_0) - f_{\min}}{\int_0^t \eta(s) ds} + \frac{\eta_0 L \sigma_0^2 N \int_0^t \eta(s)^2 ds}{2 \int_0^t \eta(s) ds}.$$

This completes the proof. ■

C.2 Proof of Proposition 4

Proof Denote $\bar{\mathbf{m}}_t := \mathbb{E}[\mathbf{m}_t]$ and $\bar{\mathbf{P}}_t := \text{Cov}(\mathbf{m}_t \mathbf{m}_t^\top)$. Then, $(\bar{\mathbf{m}}_t, \bar{\mathbf{P}}_t)$ satisfies the following ODE:

$$\begin{cases} \frac{d\bar{\mathbf{m}}_t}{dt} = -c_1 \eta(t) \bar{\mathbf{m}}_t + c_1 \eta(t) \nabla f(\mathbf{X}_t) \\ \frac{d\bar{\mathbf{P}}_t}{dt} = -2c_1 \eta(t) \bar{\mathbf{P}}_t + (c'_1)^2 \eta(t)^2 \sigma(\mathbf{X}_t) \sigma(\mathbf{X}_t)^\top. \end{cases}$$

Let $\Sigma_t := \Sigma(\mathbf{X}_t) = \sigma(\mathbf{X}_t) \sigma(\mathbf{X}_t)^\top$. The analytic solution to these equations is given by:

$$\begin{cases} \bar{\mathbf{m}}_t = \exp\left(-c_1 \int_0^t \eta(s) ds\right) \left[\int_0^t \exp\left(c_1 \int_0^s \eta(\tau) d\tau\right) c_1 \eta(s) \nabla f(\mathbf{X}_s) ds \right] \\ \bar{\mathbf{P}}_t = \exp\left(2c_1 \int_0^t \eta(s) ds\right) \left[\int_0^t \exp\left(2c_1 \int_0^s \eta(\tau) d\tau\right) (c'_1)^2 \eta(s)^2 \Sigma(\mathbf{X}_s) ds \right]. \end{cases}$$

Assumption 3.1 implies that $\sup_{\mathbf{x} \in \mathbb{R}^N} \|\nabla f(\mathbf{x})\| \leq \ell$. Therefore, we have that

$$\begin{aligned} \|\bar{\mathbf{m}}_t\| &\leq \ell \exp\left(-c_1 \int_0^t \eta(s) ds\right) \left[\int_0^t \exp\left(c_1 \int_0^s \eta(\tau) d\tau\right) c_1 \eta(s) ds \right], \\ \|\bar{\mathbf{P}}_t\|_{\text{op}} &\leq (c'_1)^2 \bar{\sigma} \exp\left(-2c_1 \int_0^t \eta(s) ds\right) \left[\int_0^t \exp\left(2c_1 \int_0^s \eta(\tau) d\tau\right) \eta(s)^2 ds \right] \\ &\leq (c'_1)^2 \bar{\sigma} \exp\left(-2c_1 \int_0^t \eta(s) ds\right) \left[\int_0^t \exp\left(2c_1 \int_0^s \eta(\tau) d\tau\right) \eta(s)^2 ds \right] \\ &\leq (c'_1)^2 \bar{\sigma} \int_0^t \eta(s)^2 ds \leq (c'_1)^2 \bar{\sigma} \Gamma < \infty, \end{aligned}$$

where $\Gamma := \int_0^\infty \eta(s)^2 ds$. By L'Hopital's rule, we have that

$$\begin{aligned} &\lim_{t \rightarrow \infty} \exp\left(-c_1 \int_0^t \eta(s) ds\right) \left[\int_0^t \exp\left(c_1 \int_0^s \eta(\tau) d\tau\right) c_1 \eta(s) ds \right] \\ &= \lim_{t \rightarrow \infty} \frac{c_1 \exp\left(c_1 \int_0^t \eta(s) ds\right) \eta(t)}{c_1 \exp\left(c_1 \int_0^t \eta(s) ds\right) \eta(t)} = 1. \end{aligned}$$

Thus, we have $\limsup_t \|\bar{\mathbf{m}}_t\| \leq \ell$. Consequently, there exists a constant C such that $\sup_t \|\bar{\mathbf{m}}_t\| \leq C < \infty$. By definition, $\mathbb{E}[\mathbf{m}_t \mathbf{m}_t^\top] = \bar{\mathbf{P}}_t + \bar{\mathbf{m}}_t \bar{\mathbf{m}}_t^\top$. Therefore, for any $t \geq 0$, we have $\|\mathbb{E}[\mathbf{m}_t \mathbf{m}_t^\top]\|_{\text{op}} \leq (c'_1)^2 \bar{\sigma} \Gamma + C^2$. Note that

$$\mathbb{E} \left[\|\mathbf{m}_t\|^2 \right] = \text{Tr} \left(\mathbb{E}[\mathbf{m}_t \mathbf{m}_t^\top] \right) \leq N \left\| \mathbb{E}[\mathbf{m}_t \mathbf{m}_t^\top] \right\|_{\text{op}}.$$

This proves the boundness of $\mathbb{E}[\|\mathbf{m}_t\|^2]$. Next, we prove the boundness of \mathbf{v}_t . By (Adam-SDE), the solution of \mathbf{v}_t is given by

$$\mathbf{v}_t = \exp\left(-\int_0^t c_2 \eta(s) ds\right) \int_0^t \exp\left(\int_0^s c_2 \eta(\tau) d\tau\right) c_2 \eta(s) \mathbf{d}_s ds,$$

where $\mathbf{d}_s := \text{diag}(\boldsymbol{\Sigma}(\mathbf{X}_s))$. By L'Hopital's rule, we have

$$\begin{aligned} \limsup_{t \rightarrow \infty} \|\mathbf{v}_t\|_\infty &\leq \sup_t \|\mathbf{d}_t\|_\infty \lim_{t \rightarrow \infty} \exp\left(-\int_0^t c_2 \eta(s) ds\right) \int_0^t \exp\left(\int_0^s c_2 \eta(\tau) d\tau\right) c_2 \eta(s) ds \\ &\leq \sup_t \|\mathbf{d}_t\|_\infty = \bar{\sigma}, \end{aligned}$$

Therefore, there exists constant $V > 0$ such that $\sup_{t \geq 0} \|\mathbf{v}_t\|_\infty \leq V$. This completes the proof. \blacksquare

C.3 Proof of Theorem 2

Proof Apply Itô's formula to $\phi_1(\mathbf{X}_t, \mathbf{m}_t, \mathbf{v}_t) := f(\mathbf{X}_t) + \frac{1}{2c_1} \langle (\mathbf{v}_t + \epsilon)^{-\frac{1}{2}} \odot \mathbf{m}_t, \mathbf{m}_t \rangle$, we have

$$\begin{aligned}
& d\phi_1(\mathbf{X}_t, \mathbf{m}_t, \mathbf{v}_t) \\
&= -\eta(t) \langle \nabla f(\mathbf{X}_t), (\mathbf{v}_t + \epsilon)^{-\frac{1}{2}} \odot \mathbf{m}_t \rangle dt - \eta(t) \langle \mathbf{m}_t - \nabla f(\mathbf{X}_t), (\mathbf{v}_t + \epsilon)^{-\frac{1}{2}} \odot \mathbf{m}_t \rangle dt \\
&\quad + \frac{c_2\eta(t)}{4c_1} \langle (\mathbf{v}_t + \epsilon)^{-\frac{3}{2}} \odot \mathbf{m}_t^2, \mathbf{v}_t - \text{diag}(\boldsymbol{\Sigma}(\mathbf{X}_t)) \rangle dt + \frac{(c'_1)^2\eta(t)^2}{2c_1} \langle \text{Diag}((\mathbf{v}_t + \epsilon)^{-\frac{1}{2}}), \boldsymbol{\Sigma}(\mathbf{X}_t) \rangle dt \\
&\quad + \frac{c'_1}{c_1} \eta(t) \langle (\mathbf{v}_t + \epsilon)^{-\frac{1}{2}} \odot \mathbf{m}_t, \sigma(\mathbf{X}_t) d\mathbf{W}_t \rangle \\
&\leq - \left(1 - \frac{c_2}{4c_1}\right) \eta(t) \langle (\mathbf{v}_t + \epsilon)^{-\frac{1}{2}} \odot \mathbf{m}_t, \mathbf{m}_t \rangle dt + \frac{(c'_1)^2\eta(t)^2}{2c_1} \langle \text{Diag}((\mathbf{v}_t + \epsilon)^{-\frac{1}{2}}), \boldsymbol{\Sigma}(\mathbf{X}_t) \rangle dt \\
&\quad + \frac{c'_1}{c_1} \eta(t) \langle (\mathbf{v}_t + \epsilon)^{-\frac{1}{2}} \odot \mathbf{m}_t, \sigma(\mathbf{X}_t) d\mathbf{W}_t \rangle,
\end{aligned}$$

where the last inequality is derived by noting that $\mathbf{v}_t \geq 0$ and $(\mathbf{v}_t + \epsilon)^{-\frac{3}{2}} \odot \mathbf{v}_t \leq (\mathbf{v}_t + \epsilon)^{-\frac{1}{2}}$. Taking integral and then taking expectation, we have

$$\begin{aligned}
& \mathbb{E}[\phi_1(\mathbf{X}_t, \mathbf{m}_t, \mathbf{v}_t) - \phi_1(\mathbf{X}_0, \mathbf{m}_0, \mathbf{v}_0)] \\
&\leq - \mathbb{E} \left[\int_0^t \left(1 - \frac{c_2}{4c_1}\right) \eta(s) \langle (\mathbf{v}_s + \epsilon)^{-\frac{1}{2}} \odot \mathbf{m}_s, \mathbf{m}_s \rangle ds \right] \\
&\quad + \mathbb{E} \left[\int_0^t \frac{(c'_1)^2\eta(s)^2}{2c_1} \langle \text{Diag}((\mathbf{v}_s + \epsilon)^{-\frac{1}{2}}), \boldsymbol{\Sigma}(\mathbf{X}_s) \rangle ds \right].
\end{aligned}$$

Therefore, it holds that

$$\mathbb{E} \left[\|\mathbf{m}_t\|^2 \right] \leq \frac{\sqrt{V + \epsilon} (\phi_1(\mathbf{X}_0, \mathbf{m}_0, \mathbf{v}_0) - f_{\min})}{\left(1 - \frac{c_2}{4c_1}\right) \int_0^t \eta(s) ds} + \frac{\frac{(c'_1)^2}{2c_1} \bar{\sigma} \sqrt{V + \epsilon} \int_0^t \eta(s)^2 ds}{\left(1 - \frac{c_2}{4c_1}\right) \sqrt{\epsilon} \int_0^t \eta(s) ds}. \quad (23)$$

Next, we derive the bound for the gradient. We construct a novel Lyapunov function $\phi_2(\mathbf{X}_t, \mathbf{m}_t, \mathbf{v}_t) := f(\mathbf{X}_t) - \frac{1}{c_1} \langle \nabla f(\mathbf{X}_t), (\mathbf{v}_t + \epsilon)^{-\frac{1}{2}} \odot \mathbf{m}_t \rangle$ which links the noiseless gradient with the momentum. Applying Itô's formula to ϕ_2 yields that

$$\begin{aligned}
& d\phi_2(\mathbf{X}_t, \mathbf{m}_t, \mathbf{v}_t) \\
&= -\eta(t) \langle \nabla f(\mathbf{X}_t), (\mathbf{v}_t + \epsilon)^{-\frac{1}{2}} \odot \mathbf{m}_t \rangle dt + \frac{\eta(t)}{c_1} \langle \nabla^2 f(\mathbf{X}_t) (\mathbf{v}_t + \epsilon)^{-\frac{1}{2}} \odot \mathbf{m}_t, (\mathbf{v}_t + \epsilon)^{-\frac{1}{2}} \odot \mathbf{m}_t \rangle dt \\
&\quad + \eta(t) \langle \nabla f(\mathbf{X}_t) \odot (\mathbf{v}_t + \epsilon)^{-\frac{1}{2}}, \mathbf{m}_t - \nabla f(\mathbf{X}_t) \rangle dt - \frac{c'_1\eta(t)}{c_1} \langle \nabla f(\mathbf{X}_t) \odot (\mathbf{v}_t + \epsilon)^{-\frac{1}{2}}, \sigma(\mathbf{X}_t) d\mathbf{W}_t \rangle \\
&\quad - \frac{c_2\eta(t)}{2c_1} \langle \nabla f(\mathbf{X}_t) \odot \mathbf{m}_t \odot (\mathbf{v}_t + \epsilon)^{-\frac{3}{2}}, \mathbf{v}_t - \text{diag}(\boldsymbol{\Sigma}(\mathbf{X}_t)) \rangle dt.
\end{aligned}$$

Taking integral and taking expectation, we have

$$\begin{aligned}
& \mathbb{E} [\phi_2(\mathbf{X}_0, \mathbf{m}_0, \mathbf{v}_0) - \phi_2(\mathbf{X}_t, \mathbf{m}_t, \mathbf{v}_t)] \\
& \leq \frac{L}{c_1} \mathbb{E} \left[\int_0^t \eta(s) \left\| \mathbf{m}_s \odot (\mathbf{v}_s + \epsilon)^{-\frac{1}{2}} \right\|^2 ds \right] - \mathbb{E} \left[\int_0^t \eta(s) \left\langle \nabla f(\mathbf{X}_s) \odot (\mathbf{v}_s + \epsilon)^{-\frac{1}{2}}, \nabla f(\mathbf{X}_s) \right\rangle ds \right] \\
& \quad - \frac{c_2}{2c_1} \mathbb{E} \left[\int_0^t \eta(s) \left\langle \nabla f(\mathbf{X}_s) \odot \mathbf{m}_s \odot (\mathbf{v}_s + \epsilon)^{-\frac{3}{2}}, \mathbf{v}_s \right\rangle ds \right] \\
& \quad + \frac{c_2 \bar{\sigma}}{2c_1} \mathbb{E} \left[\int_0^t \eta(s) \left\langle \nabla f(\mathbf{X}_s) \odot \mathbf{m}_s, (\mathbf{v}_s + \epsilon)^{-\frac{3}{2}} \right\rangle ds \right] \\
& \leq \frac{L}{c_1 \epsilon} \mathbb{E} \left[\int_0^t \eta(s) \|\mathbf{m}_s\|^2 ds \right] - \frac{1}{\sqrt{V + \epsilon}} \mathbb{E} \left[\int_0^t \eta(s) \|\nabla f(\mathbf{X}_s)\|^2 ds \right] \\
& \quad + \frac{1}{4\sqrt{V + \epsilon}} \mathbb{E} \left[\int_0^t \eta(s) \|\nabla f(\mathbf{X}_s)\|^2 ds \right] + \frac{c_2^2 \sqrt{V + \epsilon}}{4c_1^2 \epsilon} \mathbb{E} \left[\int_0^t \eta(s) \|\mathbf{m}_s\|^2 ds \right] \\
& \quad + \frac{1}{4\sqrt{V + \epsilon}} \mathbb{E} \left[\int_0^t \eta(s) \|\nabla f(\mathbf{X}_s)\|^2 ds \right] + \frac{c_2^2 \bar{\sigma}^2 \sqrt{V + \epsilon}}{4\epsilon^3 c_1^2} \mathbb{E} \left[\int_0^t \eta(s) \|\mathbf{m}_s\|^2 ds \right], \\
& = \frac{L}{c_1 \epsilon} \mathbb{E} \left[\int_0^t \eta(s) \|\mathbf{m}_s\|^2 ds \right] - \frac{1}{2\sqrt{V + \epsilon}} \mathbb{E} \left[\int_0^t \eta(s) \|\nabla f(\mathbf{X}_s)\|^2 ds \right] \\
& \quad + \left(1 + \frac{\bar{\sigma}^2}{\epsilon^2} \right) \frac{c_2^2 \sqrt{V + \epsilon}}{4c_1^2 \epsilon} \mathbb{E} \left[\int_0^t \eta(s) \|\mathbf{m}_s\|^2 ds \right].
\end{aligned}$$

The last inequality comes from Cauchy-Young's inequality:

$$\begin{aligned}
& \frac{c_2}{2c_1} \left| \left\langle \nabla f(\mathbf{X}_s) \odot \mathbf{m}_s \odot (\mathbf{v}_s + \epsilon)^{-\frac{3}{2}}, \mathbf{v}_s \right\rangle \right| = \frac{c_2}{2c_1} \left| \left\langle \nabla f(\mathbf{X}_s) \odot \mathbf{v}_s \odot (\mathbf{v}_s + \epsilon)^{-\frac{3}{2}}, \mathbf{m}_s \right\rangle \right| \\
& \leq \frac{c_2}{2c_1 \sqrt{\epsilon}} \left| \left\langle \nabla f(\mathbf{X}_s), \mathbf{m}_s \right\rangle \right| \leq \frac{c_2}{2c_1 \sqrt{\epsilon}} \|\nabla f(\mathbf{X}_s)\| \|\mathbf{m}_s\| \leq \frac{1}{4\sqrt{V + \epsilon}} \|\nabla f(\mathbf{X}_s)\|^2 + \frac{c_2^2 \sqrt{V + \epsilon}}{4c_1^2 \epsilon} \|\mathbf{m}_s\|^2.
\end{aligned}$$

and similarly,

$$\frac{c_2 \bar{\sigma}}{2c_1} \left| \left\langle \nabla f(\mathbf{X}_s) \odot \mathbf{m}_s, (\mathbf{v}_s + \epsilon)^{-\frac{3}{2}} \right\rangle \right| \leq \frac{1}{4\sqrt{V + \epsilon}} \|\nabla f(\mathbf{X}_s)\|^2 + \frac{c_2^2 \bar{\sigma}^2 \sqrt{V + \epsilon}}{4\epsilon^3 c_1^2} \|\mathbf{m}_s\|^2.$$

Then, we have

$$\begin{aligned}
\mathbb{E} \left[\|\nabla f(\mathbf{X}_t)\|^2 \right] & \leq \frac{2\sqrt{V + \epsilon} (\phi_2(\mathbf{X}_0, \mathbf{m}_0, \mathbf{v}_0) - \min_t \mathbb{E} [\phi_2(\mathbf{X}_t, \mathbf{m}_t, \mathbf{v}_t)])}{\int_0^t \eta(s) ds} \\
& \quad + \left(\frac{2L\sqrt{V + \epsilon}}{c_1 \epsilon} + \left(1 + \frac{\bar{\sigma}^2}{\epsilon^2} \right) \frac{c_2^2 (V + \epsilon)}{2c_1^2 \epsilon} \right) \mathbb{E} \left[\|\mathbf{m}_t\|^2 \right].
\end{aligned}$$

Note that $\left| \mathbb{E} \left[\left\langle \nabla f(\mathbf{X}_t), (\mathbf{v}_t + \epsilon)^{-\frac{1}{2}} \odot \mathbf{m}_t \right\rangle \right] \right| \leq \frac{\ell}{\sqrt{\epsilon}} \sqrt{\mathbb{E} \left[\|\mathbf{m}_t\|^2 \right]} \leq \frac{\ell M \sqrt{N}}{\sqrt{\epsilon}}$. Combined with (23), we prove the bound for $\mathbb{E} \left[\|\nabla f(\mathbf{X}_t)\|^2 \right]$. This completes the proof. \blacksquare

Appendix D. Proofs for Escaping Probability

D.1 Proof of Proposition 5

Proof Note that $\nabla f(\mathbf{x}^*) = 0$, we have $\frac{d\bar{\mathbf{x}}_t}{dt} = \mathbf{0}$. So $\bar{\mathbf{x}}_t$ remains constant at \mathbf{x}^* , and $\nabla^2 f(\bar{\mathbf{x}}_t) \equiv \nabla^2 f(\mathbf{x}^*)$. Then, the ODE (16) comes from (SDE-GA). Let $\mathbf{p}(t) = \text{vec}(\mathbf{P}(t))$, $\mathbf{b} = \text{vec}(\boldsymbol{\Sigma})$, where $\text{vec}(\cdot)$ is the vectorization of a matrix by column order. Then (16) for $\mathbf{P}(t)$ is equivalent to the following ODE for vector-valued function $\mathbf{p}(t)$:

$$\frac{d\mathbf{p}(t)}{dt} = -\eta(t)\mathbf{Q}\mathbf{p}(t) + \eta_0\eta(t)^2\mathbf{b},$$

where $\mathbf{Q} = \mathbf{I} \otimes \mathbf{H} + \mathbf{H} \otimes \mathbf{I}$, where \otimes is the Kronecker product. Then, we have

$$\mathbf{p}(t) = \exp\left(-\int_0^t \eta(s)\mathbf{Q}ds\right) \left(\int_0^t \exp\left(\int_0^s \eta(\tau)\mathbf{Q}d\tau\right) \eta_0\eta(s)^2\mathbf{b}ds\right).$$

Note that

$$\begin{aligned} & \exp\left(\int_0^s \eta(\tau)(\mathbf{I} \otimes \mathbf{H} + \mathbf{H} \otimes \mathbf{I})d\tau\right) \text{vec}(\boldsymbol{\Sigma}) \\ &= \exp\left(\mathbf{H} \int_0^s \eta(\tau)d\tau\right) \otimes \exp\left(\mathbf{H} \int_0^s \eta(\tau)d\tau\right) \text{vec}(\boldsymbol{\Sigma}) \\ &= \text{vec}\left(\exp\left(\mathbf{H} \int_0^s \eta(\tau)d\tau\right) \boldsymbol{\Sigma} \exp\left(\mathbf{H} \int_0^s \eta(\tau)d\tau\right)\right). \end{aligned}$$

Denote $\mathbf{A}(t) := \exp\left(-\int_0^t \eta(s)\mathbf{H}ds\right)$. Then, it holds that $(\mathbf{A}(t))^{-1} := \exp\left(\int_0^t \eta(s)\mathbf{H}ds\right)$. Hence, we obtain:

$$\begin{aligned} \mathbf{p}(t) &= \exp\left(-\int_0^t \eta(s)(\mathbf{I} \otimes \mathbf{H} + \mathbf{H} \otimes \mathbf{I})ds\right) \text{vec}\left(\int_0^t ((\mathbf{A}(s))^{-1})\boldsymbol{\Sigma}((\mathbf{A}(s))^{-1})\eta_0\eta(s)^2ds\right) \\ &= \mathbf{A}(t) \otimes \mathbf{A}(t) \text{vec}\left(\int_0^t ((\mathbf{A}(s))^{-1})\boldsymbol{\Sigma}((\mathbf{A}(s))^{-1})\eta_0\eta(s)^2ds\right) \\ &= \text{vec}\left(\mathbf{A}(t) \left(\int_0^t ((\mathbf{A}(s))^{-1})\boldsymbol{\Sigma}((\mathbf{A}(s))^{-1})\eta_0\eta(s)^2ds\right) \mathbf{A}(t)\right). \end{aligned}$$

Consequently, the matrix $\mathbf{P}(t)$ is expressed as:

$$\mathbf{P}(t) = \mathbf{A}(t) \left(\int_0^t ((\mathbf{A}(s))^{-1})\boldsymbol{\Sigma}((\mathbf{A}(s))^{-1})\eta_0\eta(s)^2ds\right) \mathbf{A}(t).$$

This completes the proof. ■

D.2 Proof of Proposition 6

We first recall the Gaussian approximations for a general SDE (Särkkä and Solin, 2019). Considering the SDE with initial condition $\mathbf{x}_{t_0} = \mathbf{x}_0$:

$$d\mathbf{x}_t = \mathbf{G}(\mathbf{x}, t)dt + \mathbf{L}(\mathbf{x}, t)d\mathbf{W}_t$$

the linearization approximation of its FPK equation yields the following differential equations for $\bar{\mathbf{x}}(t) = \mathbb{E}[\mathbf{x}_t]$ and $\mathbf{P}(t) = \text{Cov}(\mathbf{x}_t)$ with the initial condition $\bar{\mathbf{x}}_{t_0} = \mathbb{E}[\mathbf{x}_0]$, $\mathbf{P}_{t_0} = \text{Cov}(\mathbf{x}_{t_0})$:

$$\begin{cases} \frac{d\bar{\mathbf{x}}}{dt} = \mathbf{G}(\bar{\mathbf{x}}, t) \\ \frac{d\mathbf{P}}{dt} = \mathbf{P}\mathbf{G}_{\mathbf{x}}^{\top}(\bar{\mathbf{x}}, t) + \mathbf{G}_{\mathbf{x}}(\bar{\mathbf{x}}, t)\mathbf{P} + \mathbf{L}(\bar{\mathbf{x}}, t)\mathbf{L}(\bar{\mathbf{x}}, t)^{\top}. \end{cases} \quad (\text{general-GA})$$

Proof Let $\mathbf{Z}_0 := [\mathbf{X}_0; \mathbf{m}_0; \mathbf{v}_0] = [\mathbf{x}^*; \mathbf{0}; \text{diag}(\boldsymbol{\Sigma}(\mathbf{x}^*))]$. Then $\bar{\mathbf{z}}_0 = \mathbf{Z}_0$ is a zero of $\mathbf{F}(\mathbf{Z})$ defined in (18). Therefore, the trajectory $\bar{\mathbf{z}}_t$ remains at \mathbf{Z}_0 . Note that $\frac{\partial F(\mathbf{Z}_0)}{\partial \mathbf{Z}} = \widehat{\mathbf{H}}$. Then (20) can be derived by substituting $\bar{\mathbf{z}}_t = \mathbf{Z}_0$, (18) and (19) into (general-GA). The remainder of the proof follows similarly to that of Proposition 5, and thus is omitted for brevity. ■

D.3 Anti-concentration for Gaussian

Before proving the main results for the escape probability, we need a general anti-concentration inequality for Gaussian variables, as considered in other scenarios (Carbery and Wright, 2001; Tu and Boczar, 2023).

Lemma 1 *Assume $\mathbf{x} \sim \mathcal{N}(\boldsymbol{\mu}, \boldsymbol{\Sigma})$, for any $\varepsilon \in (0, \text{Tr}(\boldsymbol{\Sigma}))$, we have*

$$\mathbb{P}\left[\|\mathbf{x} - \boldsymbol{\mu}\|^2 \leq \varepsilon\right] \leq \sqrt{\frac{e\varepsilon}{\text{Tr}(\boldsymbol{\Sigma})}}.$$

Proof Applying Chernoff's bound, we have:

$$\begin{aligned} \mathbb{P}\left[\|\mathbf{x} - \boldsymbol{\mu}\|^2 \leq \varepsilon\right] &\leq \inf_{\lambda > 0} \left\{ \exp(\lambda\varepsilon) \int_{\mathbb{R}^N} \frac{1}{\sqrt{(2\pi)^N \det^*(\boldsymbol{\Sigma})}} \exp\left(-\lambda\|\mathbf{x}\|^2 - \frac{1}{2}\mathbf{x}^{\top}\boldsymbol{\Sigma}^{\dagger}\mathbf{x}\right) d\mathbf{x} \right\} \\ &= \inf_{\lambda > 0} \left\{ \exp(\lambda\varepsilon) \int_{\mathbb{R}^N} \frac{1}{\sqrt{(2\pi)^N \det^*(\boldsymbol{\Sigma})}} \exp\left(-\frac{1}{2}\mathbf{x}^{\top}(2\lambda\mathbf{I}_N + \boldsymbol{\Sigma}^{\dagger})\mathbf{x}\right) d\mathbf{x} \right\} \\ &= \inf_{\lambda > 0} \left\{ \exp(\lambda\varepsilon) \sqrt{\frac{(2\pi)^N \det\left((2\lambda\mathbf{I}_N + \boldsymbol{\Sigma}^{\dagger})^{-1}\right)}{(2\pi)^N \det^*(\boldsymbol{\Sigma})}} \right\} = \inf_{\lambda > 0} \left\{ \exp(\lambda\varepsilon) \frac{1}{\sqrt{\det(2\lambda\boldsymbol{\Sigma} + \mathbf{I}_N)}} \right\} \\ &\stackrel{(a)}{\leq} \inf_{\lambda > 0} \left\{ \exp(\lambda\varepsilon) \frac{1}{\sqrt{1 + 2\lambda \text{Tr}(\boldsymbol{\Sigma})}} \right\} \stackrel{(b)}{=} \sqrt{\frac{\varepsilon}{\text{Tr}(\boldsymbol{\Sigma})}} \exp\left(\frac{\text{Tr}(\boldsymbol{\Sigma}) - \varepsilon}{2\text{Tr}(\boldsymbol{\Sigma})}\right) \leq \sqrt{\frac{e\varepsilon}{\text{Tr}(\boldsymbol{\Sigma})}}, \end{aligned}$$

where $\boldsymbol{\Sigma}^{\dagger}$ is the Moore-Penrose pseudoinverse of $\boldsymbol{\Sigma}$ and $\det^*(\cdot)$ is the pseudo-determinant. In the above, (a) comes from

$$\det(2\lambda\boldsymbol{\Sigma} + \mathbf{I}_N) = \prod_{i=1}^N (1 + 2\lambda\sigma_i) \geq 1 + 2\lambda \sum_{i=1}^N \sigma_i = 1 + 2\lambda \text{Tr}(\boldsymbol{\Sigma}).$$

where σ_i is the i -th eigenvalue of $\boldsymbol{\Sigma}$, and (b) is optimized by setting $\lambda = \frac{\text{Tr}(\boldsymbol{\Sigma}) - \varepsilon}{2\varepsilon \text{Tr}(\boldsymbol{\Sigma})}$. ■

D.4 Proof of Theorem 3

Proof Let \mathbf{U} be an orthogonal matrix such that $\mathbf{H} = \mathbf{U}\mathbf{\Lambda}\mathbf{U}^\top$, where $\mathbf{\Lambda}$ is the diagonal matrix of eigenvalues of \mathbf{H} . Let λ_{\max} be the maximal eigenvalue of \mathbf{H} . By equation (17), we have that

$$\begin{aligned} \text{Tr}(\mathbf{P}(t)) &= \text{Tr} \left(\int_0^t \exp \left(-\mathbf{H} \int_s^t \eta(\tau) d\tau \right) \mathbf{\Sigma} \exp \left(-\mathbf{H} \int_s^t \eta(\tau) d\tau \right) \eta_0 \eta(s)^2 ds \right) \\ &= \text{Tr} \left(\int_0^t \exp \left(-\mathbf{\Lambda} \int_s^t \eta(\tau) d\tau \right) \mathbf{U}^\top \mathbf{\Sigma} \mathbf{U} \exp \left(-\mathbf{\Lambda} \int_s^t \eta(\tau) d\tau \right) \eta_0 \eta(s)^2 ds \right) \\ &\geq \eta_0 \text{Tr}(\mathbf{\Sigma}) \int_0^t \exp \left(-2\lambda_{\max} \int_s^t \eta(\tau) d\tau \right) \eta(s)^2 ds \\ &\geq \eta_0 \text{Tr}(\mathbf{\Sigma}) \int_0^t \exp(-2\lambda_{\max} \eta_{\max}(t-s)) \eta(s)^2 ds \\ &\geq C \eta_0 \text{Tr}(\mathbf{\Sigma}) \int_0^t \eta(s)^2 ds, \end{aligned}$$

where $C := \inf_{t \geq 0} \frac{\int_0^t \exp(-2\lambda_{\max} \eta_{\max}(t-s)) \eta(s)^2 ds}{\int_0^t \eta(s)^2 ds}$. Next, we demonstrate that $C > 0$ by considering two cases. When $\int_0^\infty \eta(s)^2 ds < \infty$, it is clear that $C > 0$. When $\int_0^\infty \eta(s)^2 ds = \infty$, by L'Hopital's rule, we have

$$\lim_{t \rightarrow \infty} \frac{\int_0^t \exp(-2\lambda_{\max} \eta_{\max}(t-s)) \eta(s)^2 ds}{\int_0^t \eta(s)^2 ds} = \lim_{t \rightarrow \infty} \frac{\eta(t)^2}{\eta(t)^2} = 1.$$

Thus, $C > 0$. The condition $\eta(0) = \eta_{\max}$ and $\eta(T) = 0$ leads to the following inequality derived from the Cauchy-Schwarz inequality:

$$\left(\int_0^T \eta(s)^2 ds \right) \left(\int_0^T \eta'(s)^2 ds \right) \geq \left(\int_0^T \eta(s) \eta'(s) ds \right)^2.$$

Integrating by parts yields:

$$\int_0^T \eta(s) \eta'(s) ds = \eta(s)^2 \Big|_0^T - \int_0^T \eta(s) \eta'(s) ds,$$

which results in

$$\int_0^T \eta(s) \eta'(s) ds = -\frac{\eta_{\max}^2}{2}.$$

This result leads to the following inequality:

$$\frac{\left(\frac{\eta_{\max}^2}{2} \right)^2}{\int_0^T \eta(s)^2 ds} \leq \int_0^T \eta'(s)^2 ds.$$

Now, suppose Assumption 2 holds. For any fix $\delta \in (0, 1)$, by Proposition 2 and setting $t = \delta \text{Tr}(\mathbf{\Sigma}_g)$, we have

$$\begin{aligned} &\mathbb{P} \{ (1 - \delta) \text{Tr}(\mathbf{\Sigma}_g) \leq \text{Tr}(\mathbf{\Sigma}(\mathbf{x})) \leq (1 + \delta) \text{Tr}(\mathbf{\Sigma}_g) \} \\ &\geq 1 - 2 \exp \left\{ -\frac{D\delta^2 (\text{Tr}(\mathbf{\Sigma}_g))^2}{4 \text{Tr}(\mathbf{\Sigma}_g^2) + 2\delta \text{Tr}(\mathbf{\Sigma}_g) \|\mathbf{\Sigma}_g\|_{\text{op}}} \right\}. \end{aligned}$$

Denote the event $\mathcal{E} := \{(1-\delta) \text{Tr}(\mathbf{\Sigma}_g) \leq \text{Tr}(\mathbf{\Sigma}(\mathbf{x})) \leq (1+\delta) \text{Tr}(\mathbf{\Sigma}_g)\}$ and $\mathcal{A} := \{\|\mathbf{X}_T - \mathbf{x}^*\|^2 \leq \varepsilon\}$. By Proposition 5, $\mathbb{E}[\mathbf{X}_T] = \bar{\mathbf{x}}_T = \mathbf{x}^*$. Then, applying Lemma 1, we get

$$\begin{aligned} \mathbb{P}\left\{\|\mathbf{X}_T - \mathbf{x}^*\|^2 \leq \varepsilon \mid \mathcal{E}\right\} &\leq \sqrt{\frac{e\varepsilon}{\text{Tr}(\mathbf{P}_t)}} \leq \sqrt{\frac{e\varepsilon}{C\eta_0 \text{Tr}(\mathbf{\Sigma}) \left(\frac{\eta_{\max}^2}{2}\right)^2} \int_0^T \eta'(s)^2 ds} \\ &\leq \sqrt{\frac{e\varepsilon}{C\eta_0(1-\delta) \text{Tr}(\mathbf{\Sigma}_g) \left(\frac{\eta_{\max}^2}{2}\right)^2} \int_0^T \eta'(s)^2 ds}. \end{aligned}$$

Finally, we have

$$\begin{aligned} \mathbb{P}\{\mathcal{A}\} &= \mathbb{P}\{\mathcal{A} \mid \mathcal{E}\} \mathbb{P}\{\mathcal{E}\} + \mathbb{P}\{\mathcal{A} \mid \mathcal{E}^c\} \mathbb{P}\{\mathcal{E}^c\} \leq \mathbb{P}\{\mathcal{A} \mid \mathcal{E}\} + \mathbb{P}\{\mathcal{E}^c\} \\ &\leq \sqrt{\frac{e\varepsilon}{C\eta_0(1-\delta) \text{Tr}(\mathbf{\Sigma}_g) \left(\frac{\eta_{\max}^2}{2}\right)^2} \int_0^T \eta'(s)^2 ds} + 2 \exp\left\{-\frac{D\delta^2 (\text{Tr}(\mathbf{\Sigma}_g))^2}{4 \text{Tr}(\mathbf{\Sigma}_g^2) + 2\delta \text{Tr}(\mathbf{\Sigma}_g) \|\mathbf{\Sigma}_g\|_{\text{op}}}\right\}. \end{aligned}$$

Since $D \gg N$, the second term is sufficiently small compared with the first term. Finally, we derive the bound

$$\mathbb{P}[\|\mathbf{X}_T - \mathbf{x}^*\|^2 \leq \varepsilon] = \mathcal{O}\left(\left(\frac{\varepsilon}{\eta_{\max}^4 \sigma_g^2} \int_0^T \eta'(s)^2 ds\right)^{1/2}\right).$$

This completes the proof. \blacksquare

D.5 Proof of Theorem 4

Proof The proof follows similarly to the proof of Theorem 3, and hence we omit the details. \blacksquare

References

- J. Achiam, S. Adler, S. Agarwal, L. Ahmad, I. Akkaya, F. L. Aleman, et al. GPT-4 technical report. *arXiv preprint arXiv:2303.08774*, 2023.
- C. Archambeau, D. Cornford, M. Opper, and J. Shawe-Taylor. Gaussian process approximations of stochastic differential equations. *Journal of Machine Learning Research*, 1:1–16, 2007.
- Y. Arjevani, Y. Carmon, J. C. Duchi, D. J. Foster, N. Srebro, and B. Woodworth. Lower bounds for non-convex stochastic optimization. *Mathematical Programming*, pages 1–50, 2022.
- H. Attouch, Z. Chbani, J. Peypouquet, and P. Redont. Fast convergence of inertial dynamics and algorithms with asymptotic vanishing viscosity. *Mathematical Programming*, 168: 123–175, 2018.

- H. Attouch, Z. Chbani, and H. Riahi. Fast convex optimization via a third-order in time evolution equation: Toges-v an improved version of toges. *Optimization*, 73(3):575–595, 2024.
- J. Bai, S. Bai, Y. Chu, Z. Cui, K. Dang, X. Deng, et al. Qwen technical report. *arXiv preprint arXiv:2309.16609*, 2023.
- Z. Bai and J. W. Silverstein. *Spectral analysis of large dimensional random matrices*, volume 20. Springer, 2010.
- B. Battash, L. Wolf, and O. Lindenbaum. Revisiting the noise model of stochastic gradient descent. In *International Conference on Artificial Intelligence and Statistics*, pages 4780–4788. PMLR, 2024.
- N. Berglund. Kramers’ law: Validity, derivations and generalisations. *Markov Processes And Related Fields*, 19(3):459–490, 2013.
- N. Berglund and B. Gentz. Sharp estimates for metastable lifetimes in parabolic SPDEs: Kramers’ law and beyond. *Electronic Journal of Probability*, 18(24):1–58, 2013.
- D. P. Bertsekas and J. N. Tsitsiklis. Gradient convergence in gradient methods with errors. *SIAM Journal on Optimization*, 10(3):627–642, 2000.
- T. Besiroglu, E. Erdil, M. Barnett, and J. You. Chinchilla Scaling: A replication attempt. *arXiv preprint arXiv:2404.10102*, 2024.
- X. Bi, D. Chen, G. Chen, S. Chen, D. Dai, C. Deng, et al. DeepSeek LLM: Scaling open-source language models with longtermism. *arXiv preprint arXiv:2401.02954*, 2024.
- A. Bovier and F. Den Hollander. Metastability: a potential-theoretic approach. *Grundlehren der mathematischen Wissenschaften*, 351, 2015.
- E. Caballero, K. Gupta, I. Rish, and D. Krueger. Broken neural scaling laws. In *The Eleventh International Conference on Learning Representations*, 2023.
- A. Carbery and J. Wright. Distributional and L^q norm inequalities for polynomials over convex bodies in \mathbb{R}^n . *Mathematical Research Letters*, 8(3):233–248, 2001.
- T. Computer. RedPajama: An open dataset for training large language models, 2023. URL <https://github.com/togethercomputer/RedPajama-Data>.
- M. Dambrine, C. Dossal, B. Puig, and A. Rondepierre. Stochastic differential equations for modeling first order optimization methods. *SIAM Journal on Optimization*, 34(2):1402–1426, 2024.
- D. Davis, D. Drusvyatskiy, S. Kakade, and J. D. Lee. Stochastic subgradient method converges on tame functions. *Foundations of Computational Mathematics*, 20(1):119–154, 2020.

- DeepSeek-AI, A. Liu, B. Feng, B. Wang, B. Wang, B. Liu, et al. DeepSeek-V2: A strong, economical, and efficient mixture-of-experts language model. *arXiv preprint arXiv:2405.04434*, 2024.
- K. Ding and K.-C. Toh. Stochastic Bregman Subgradient Methods for Nonsmooth Nonconvex Optimization Problems. *arXiv preprint arXiv:2404.17386*, 2024.
- K. Ding, N. Xiao, and K.-C. Toh. Adam-family methods with decoupled weight decay in deep learning. *arXiv preprint arXiv:2310.08858*, 2023.
- A. Dubey, A. Jauhri, A. Pandey, A. Kadian, A. Al-Dahle, A. Letman, et al. The LLaMA 3 herd of models. *arXiv preprint arXiv:2407.21783*, 2024.
- J. C. Duchi and F. Ruan. Stochastic methods for composite and weakly convex optimization problems. *SIAM Journal on Optimization*, 28(4):3229–3259, 2018.
- P. Foret, A. Kleiner, H. Mobahi, and B. Neyshabur. Sharpness-aware minimization for efficiently improving generalization. *arXiv preprint arXiv:2010.01412*, 2020.
- L. Gao, J. Schulman, and J. Hilton. Scaling laws for reward model overoptimization. In *International Conference on Machine Learning*, pages 10835–10866. PMLR, 2023.
- B. Gess and S. Kassing. Convergence rates for momentum stochastic gradient descent with noise of machine learning type. *arXiv preprint arXiv:2302.03550*, 2023.
- I. I. Gihman and A. V. Skorohod. *Stochastic Differential Equations*. Springer New York, 1979.
- S. Goyal, P. Maini, Z. C. Lipton, A. Raghunathan, and J. Z. Kolter. Scaling laws for data filtering—data curation cannot be compute agnostic. In *Proceedings of the IEEE/CVF Conference on Computer Vision and Pattern Recognition*, pages 22702–22711, 2024.
- B. Grimmer, K. Shu, and A. Wang. Accelerated objective gap and gradient norm convergence for gradient descent via long steps. *arXiv preprint arXiv:2403.14045*, 2024.
- Y. Guo, J. Fu, H. Zhang, D. Zhao, and Y. Shen. Efficient continual pre-training by mitigating the stability gap. *arXiv preprint arXiv:2406.14833*, 2024.
- Z. Guo, Y. Xu, W. Yin, R. Jin, and T. Yang. A novel convergence analysis for algorithms of the Adam family. *arXiv preprint arXiv:2112.03459*, 2021.
- K. Gupta, B. Thérien, A. Ibrahim, M. L. Richter, Q. G. Anthony, E. Belilovsky, et al. Continual pre-training of large language models: How to re-warm your model? In *Workshop on Efficient Systems for Foundation Models@ ICML*, 2023.
- A. Hägele, E. Bakouch, A. Kosson, L. B. Allal, L. Von Werra, and M. Jaggi. Scaling laws and compute-optimal training beyond fixed training durations. *arXiv preprint arXiv:2405.18392*, 2024.
- F. He, T. Liu, and D. Tao. Control batch size and learning rate to generalize well: Theoretical and empirical evidence. *Advances in Neural Information Processing Systems*, 32, 2019.

- D. Hernandez, J. Kaplan, T. Henighan, and S. McCandlish. Scaling laws for transfer. *arXiv preprint arXiv:2102.01293*, 2021.
- J. Hoffmann, S. Borgeaud, A. Mensch, E. Buchatskaya, T. Cai, E. Rutherford, et al. Training compute-optimal large language models. *arXiv preprint arXiv:2203.15556*, 2022.
- S. Hu, Y. Tu, X. Han, C. He, G. Cui, X. Long, et al. Minicpm: Unveiling the potential of small language models with scalable training strategies. *arXiv preprint arXiv:2404.06395*, 2024.
- H. Ibayashi and M. Imaizumi. Why does sgd prefer flat minima?: Through the lens of dynamical systems. In *When Machine Learning meets Dynamical Systems: Theory and Applications*, 2023.
- A. Ibrahim, B. Thérien, K. Gupta, M. L. Richter, Q. Anthony, T. Lesort, et al. Simple and scalable strategies to continually pre-train large language models. *arXiv preprint arXiv:2403.08763*, 2024.
- B. Isik, N. Ponomareva, H. Hazimeh, D. Paparas, S. Vassilvitskii, and S. Koyejo. Scaling laws for downstream task performance of large language models. *arXiv preprint arXiv:2402.04177*, 2024.
- S. Jastrzębski, Z. Kenton, D. Arpit, N. Ballas, A. Fischer, et al. Three factors influencing minima in SGD. *arXiv preprint arXiv:1711.04623*, 2017.
- H. Jin, W. Wei, X. Wang, W. Zhang, and Y. Wu. Rethinking learning rate tuning in the era of large language models. *arXiv preprint arXiv:2309.08859*, 2023.
- J. Kaplan, S. McCandlish, T. Henighan, T. B. Brown, B. Chess, R. Child, et al. Scaling laws for neural language models. *arXiv preprint arXiv:2001.08361*, 2020.
- Z. Ke, Y. Shao, H. Lin, T. Konishi, G. Kim, and B. Liu. Continual pre-training of language models. *arXiv preprint arXiv:2302.03241*, 2023.
- N. S. Keskar, D. Mudigere, J. Nocedal, M. Smelyanskiy, and P. T. P. Tang. On large-batch training for deep learning: Generalization gap and sharp minima. *arXiv preprint arXiv:1609.04836*, 2016.
- G. Khromov and S. P. Singh. Some fundamental aspects about Lipschitz continuity of neural networks. In *The Twelfth International Conference on Learning Representations*, 2024.
- H. Kim, G. Papamakarios, and A. Mnih. The Lipschitz constant of self-attention. In *International Conference on Machine Learning*, pages 5562–5571. PMLR, 2021.
- D. P. Kingma and J. Ba. Adam: A method for stochastic optimization. *arXiv preprint arXiv:1412.6980*, 2014.
- P. E. Kloeden and E. Platen. *Numerical Solution to Stochastic Differential Equations*. Springer, 1999.

- H. A. Kramers. Brownian motion in a field of force and the diffusion model of chemical reactions. *Physical*, 7(4):284–304, 1940.
- M. Ledoux and B. Rider. Small deviations for beta ensembles. *Electronic Journal of Probability*, 15(41):1319–1343, 2010.
- H. Li and Z. Lin. Restarted nonconvex accelerated gradient descent: No more polylogarithmic factor in the $\mathcal{O}(\epsilon^{-7/4})$ complexity. In *International Conference on Machine Learning*, pages 12901–12916. PMLR, 2022.
- Q. Li, C. Tai, and E. Weinan. Stochastic modified equations and adaptive stochastic gradient algorithms. In *International Conference on Machine Learning*, pages 2101–2110. PMLR, 2017.
- Q. Li, C. Tai, and E. Weinan. Stochastic modified equations and dynamics of stochastic gradient algorithms i: Mathematical foundations. *Journal of Machine Learning Research*, 20(40):1–47, 2019.
- Z. Li, S. Malladi, and S. Arora. On the validity of modeling SGD with stochastic differential equations (SDEs). *Advances in Neural Information Processing Systems*, 34:12712–12725, 2021.
- I. Loshchilov and F. Hutter. Decoupled weight decay regularization. *arXiv preprint arXiv:1711.05101*, 2017.
- K. Lv, Y. Yang, T. Liu, Q. Gao, Q. Guo, and X. Qiu. Full parameter fine-tuning for large language models with limited resources. *arXiv preprint arXiv:2306.09782*, 2023.
- S. Malladi, K. Lyu, A. Panigrahi, and S. Arora. On the SDEs and scaling rules for adaptive gradient algorithms. In *Advances in Neural Information Processing Systems*, 2022.
- R. Maulen-Soto, J. Fadili, and H. Attouch. An SDE perspective on stochastic convex optimization. *arXiv preprint arXiv:2207.02750*, 2022.
- R. Maulen-Soto, J. Fadili, H. Attouch, and P. Ochs. An SDE perspective on stochastic inertial gradient dynamics with time-dependent viscosity and geometric damping. *arXiv preprint arXiv:2407.04562*, 2024.
- R. May. Asymptotic for a second-order evolution equation with convex potential and vanishing damping term. *Turkish Journal of Mathematics*, 41(3):681–685, 2017.
- T. Mori, L. Ziyin, K. Liu, and M. Ueda. Power-law escape rate of SGD. In *International Conference on Machine Learning*, pages 15959–15975. PMLR, 2022.
- M. Muehlebach and M. Jordan. A dynamical systems perspective on Nesterov acceleration. In *International Conference on Machine Learning*, pages 4656–4662. PMLR, 2019.
- N. Muennighoff, A. Rush, B. Barak, T. Le Scao, N. Tazi, A. Piktus, et al. Scaling data-constrained language models. *Advances in Neural Information Processing Systems*, 36, 2024.

- Y. Nesterov. A method for solving the convex programming problem with convergence rate $O(1/k^2)$. In *Dokl akad nauk Sssr*, volume 269, page 543, 1983.
- T. H. Nguyen, U. Simsekli, M. Gurbuzbalaban, and G. Richard. First exit time analysis of stochastic gradient descent under heavy-tailed gradient noise. *Advances in Neural Information Processing Systems*, 32, 2019.
- J. Parmar, S. Satheesh, M. Patwary, M. Shoeybi, and B. Catanzaro. Reuse, don't retrain: A recipe for continued pretraining of language models. *arXiv preprint arXiv:2407.07263*, 2024.
- B. Polyak. *Introduction to Optimization*. Optimization Software, New York, 1987.
- S. J. Reddi, S. Kale, and S. Kumar. On the convergence of adam and beyond. In *International Conference on Learning Representations*, 2018.
- M. Reid, N. Savinov, D. Teplyashin, D. Lepikhin, T. Lillicrap, J.-b. Alayrac, et al. Gemini 1.5: Unlocking multimodal understanding across millions of tokens of context. *arXiv preprint arXiv:2403.05530*, 2024.
- J. S. Rosenfeld, A. Rosenfeld, Y. Belinkov, and N. Shavit. A constructive prediction of the generalization error across scales. In *International Conference on Learning Representations*, 2020.
- T. Rotaru, F. Glineur, and P. Patrinos. Exact worst-case convergence rates of gradient descent: a complete analysis for all constant stepsizes over nonconvex and convex functions. *arXiv preprint arXiv:2406.17506*, 2024.
- N. Sardana, J. Portes, S. Doubov, and J. Frankle. Beyond Chinchilla-optimal: Accounting for inference in language model scaling laws. In *International Conference on Machine Learning*, 2024.
- S. Särkkä and J. Sarmavuori. Gaussian filtering and smoothing for continuous-discrete dynamic systems. *Signal Processing*, 93(2):500–510, 2013.
- S. Särkkä and A. Solin. *Applied Stochastic Differential Equations*, volume 10. Cambridge University Press, 2019.
- S. Särkkä, J. Hartikainen, I. S. Mbalawata, and H. Haario. Posterior inference on parameters of stochastic differential equations via non-linear gaussian filtering and adaptive MCMC. *Statistics and Computing*, 25(2):427–437, 2015.
- H. Shen and T. Chen. A single-timescale analysis for stochastic approximation with multiple coupled sequences. *Advances in Neural Information Processing Systems*, 35:17415–17429, 2022.
- D. Shrivastava, D. Kocetkov, H. de Vries, D. Bahdanau, and T. Scholak. Repofusion: Training code models to understand your repository. *arXiv preprint arXiv:2306.10998*, 2023.

- U. Simsekli, L. Sagun, and M. Gurbuzbalaban. A tail-index analysis of stochastic gradient noise in deep neural networks. In *International Conference on Machine Learning*, pages 5827–5837. PMLR, 2019.
- A. Solin, E. Tamir, and P. Verma. Scalable inference in SDEs by direct matching of the Fokker–Planck–Kolmogorov equation. *Advances in Neural Information Processing Systems*, 34:417–429, 2021.
- R. M. Soto, J. Fadili, and H. Attouch. An SDE perspective on stochastic convex optimization. *arXiv preprint arXiv:2207.02750*, 2022.
- W. Su, S. Boyd, and E. Candes. A differential equation for modeling Nesterov’s accelerated gradient method: Theory and insights. *Advances in Neural Information Processing Systems*, 27, 2014.
- S. Tu and R. Boczar. An elementary proof of anti-concentration for degree two non-negative gaussian polynomials. *arXiv preprint arXiv:2301.05992*, 2023.
- T. Wei, B. Zhu, L. Zhao, C. Cheng, B. Li, W. Lü, et al. Skywork-MoE: A deep dive into training techniques for mixture-of-experts language models. *arXiv preprint arXiv:2406.06563*, 2024.
- N. Xiao, X. Hu, and K.-C. Toh. Convergence guarantees for stochastic subgradient methods in nonsmooth nonconvex optimization. *arXiv preprint arXiv:2307.10053*, 2023.
- N. Xiao, X. Hu, X. Liu, and K.-C. Toh. Adam-family methods for nonsmooth optimization with convergence guarantees. *Journal of Machine Learning Research*, 25(48):1–53, 2024.
- X. Xie, Q. Wang, Z. Ling, X. Li, G. Liu, and Z. Lin. Optimization induced equilibrium networks: An explicit optimization perspective for understanding equilibrium models. *IEEE Transactions on Pattern Analysis and Machine Intelligence*, 45(3):3604–3616, 2022.
- X. Xie, Z. Lin, K.-C. Toh, and P. Zhou. LoCo: Low-bit communication adaptor for large-scale model training. *arXiv preprint arXiv:2407.04480*, 2024a.
- X. Xie, P. Zhou, H. Li, Z. Lin, and S. Yan. Adan: Adaptive Nesterov momentum algorithm for faster optimizing deep models. *IEEE Transactions on Pattern Analysis and Machine Intelligence*, 2024b.
- Z. Xie, I. Sato, and M. Sugiyama. A diffusion theory for deep learning dynamics: Stochastic gradient descent exponentially favors flat minima. In *International Conference on Learning Representations*, 2020.
- A. Yang, B. Yang, B. Hui, B. Zheng, B. Yu, C. Zhou, et al. Qwen2 technical report. *arXiv preprint arXiv:2407.10671*, 2024.
- H. Zhang, C. Wei, J. Lee, and T. Ma. Shape matters: Understanding the implicit bias of the noise covariance. In *Conference on Learning Theory*, pages 2315–2357. PMLR, 2021.

- L. Zhao, T. Wei, L. Zeng, C. Cheng, L. Yang, P. Cheng, et al. LongSkywork: A training recipe for efficiently extending context length in large language models. *arXiv preprint arXiv:2406.00605*, 2024.
- P. Zhou, X. Xie, Z. Lin, K.-C. Toh, and S. Yan. Win: Weight-decay-integrated Nesterov acceleration for faster network training. *Journal of Machine Learning Research*, 25(83): 1–74, 2024a.
- P. Zhou, X. Xie, Z. Lin, and S. Yan. Towards understanding convergence and generalization of AdamW. *IEEE Transactions on Pattern Analysis and Machine Intelligence*, 2024b.
- Z. Zhu, J. Wu, B. Yu, L. Wu, and J. Ma. The anisotropic noise in stochastic gradient descent: Its behavior of escaping from sharp minima and regularization effects. In *International Conference on Machine Learning*, pages 7654–7663. PMLR, 2019.